Geochemical and spectral characterization of an altered Antarctic dolerite: Implications for recent weathering on Mars

V.F. Chevrier, R. Roy, P.Y. Meslin, S. Le Mouélic, P.E. Mathé, P. Rochette, G. Bonello

Geochemical and spectral characterization of an altered Antarctic dolerite: Implications for recent weathering on Mars

V.F. Chevrier [a,*], R. Roy [b], P.Y. Meslin [c], S. Le Mouélic [d], P.E. Mathé [e], P. Rochette [e], G. Bonello [f]

[a] Arkansas Center for Space and Planetary Sciences, University of Arkansas, 332 N. Arkansas Ave., Fayetteville, AR, 72701, USA
[b] Orano Canada Inc., 817 - 45th Street West, Saskatoon, SK, S7L 5X2, Canada
[c] Institut de Recherche en Astrophysique et Planétologie, UPS-CNRS-OMP, 9 Avenue Du Colonel Roche, BP46, 31028, Toulouse Cedex 04, France
[d] CNRS, Université de Nantes, Laboratoire de Planétologie et Géodynamique, UMR 6112, 2 Rue de la Houssinière, Nantes, F-44000, France
[e] Aix Marseille Univ, CNRS, Coll France, IRD, INRAE, CEREGE, Aix-en-Provence, France
[f] LED's CHAT - Digital Art for Interior Design and Communication, Marseille 04, Provence-Alpes-Côte D'Azur, France

ARTICLE INFO

Keywords:
Antarctica
Ferrar dolerite
Mars
Regolith
Weathering
Reflectance spectroscopy
LIBS

ABSTRACT

We present new mineralogical, chemical and spectral analysis of an alteration profile on the Ferrar dolerite (Dry Valley, Antarctica), complementing a previous study (Chevrier et al., 2006a). The whole profile is about 5 cm long and subdivided into three different layers: a brown surface rind inferior to 1 mm in thickness, followed by a brownish-grey discoloration zone from 1 to 5 mm depth and finally a dark fresh core. Mineralogical (X-Ray Diffraction), chemical (EDAX, LIBS), and spectral (FTIR) measurements indicate the formation of iron (oxy)-hydroxides (maghemite) in the very top millimeter of the alteration profile, resulting from the destabilization of ferromagnesian minerals (pyroxene). This zone also exhibits strong hydration features as evidenced by LIBS hydrogen signal and the 2.80 μm water band in reflectance spectra. Below this alteration zone (around 5-mm-deep), spectral measurements indicate a discolored zone characterized by an enrichment in pyroxene (1.00 and 2.00 μm bands), possibly due to the dissolution of the glass component in the matrix. However, despite these spectral changes, the overall chemistry and mineralogy of the sample remains largely unaffected. This suggests that recent cold and dry weathering on the surface of Mars may spectrally modify surfaces of basaltic rocks, by forming iron (and manganese) (oxy)-hydroxides, but essentially in the very uppermost millimeter and that the underlying mineralogy should remain intact.

1. Introduction

The surface of Mars is globally covered by an oxidized regolith made of fine dust particles mixed with basaltic sands, rocks, and salts (Goetz et al., 2010). Spectroscopic observations from orbiters and landers showed an abundance of ferric iron nanophase (oxy)-hydroxides in the Martian regolith (Bell III et al., 2000; Poulet et al., 2007). Various phases may describe the spectroscopic properties including nanophase red hematite (Morris et al., 1989), goethite (Morris and Golden, 1998), ferrihydrite (Bishop et al., 1998) and iron-rich clays (Banin et al., 1993; Bishop et al., 1995). Mössbauer analyses performed by the Mars Exploration Rovers (MER) indicate the presence of abundant paramagnetic and poorly crystalline (oxy)-hydroxides in the Martian regolith (Morris et al., 2004) mixed with several percent of a strongly magnetic phases such as magnetite or maghemite (Goetz et al., 2005). X-Ray Diffraction (XRD) analyses of the Martian soil in Gale crater revealed the presence of a few percent of magnetite and hematite (Bish et al., 2013). Both minerals are mixed with an abundant amorphous component of yet unknown nature, which is enriched in volatile species (Blake et al., 2013; Leshin et al., 2013; Meslin et al., 2013) and whose composition is compatible with the presence of hisingerite (or silica + ferrihydrite) and nanophase ferric oxides (Dehouck et al., 2014).

Various mechanisms may explain such a coexistence of strongly colored and magnetic iron phase(s), including palagonitisation by hydrothermal or surface liquid water (Newsom et al., 1999), weathering by atmospheric components (Chevrier et al., 2004; Dehouck et al., 2012), direct oxidation of the basaltic surface (Bibring et al., 2006; Salvatore et al., 2014), and impact-induced alteration of iron-rich clay deposits (Gavin and Chevrier, 2010). Depending on the mechanism, the strongly magnetic phases can be inherited from the primary bedrock or

* Corresponding author.
E-mail address: vchevrie@uark.edu (V.F. Chevrier).

newly-formed during the alteration process. Beyond the mechanism(s) leading to the regolith formation, the environmental conditions such as temperature, pressure and particularly the amount of liquid water can strongly affect the outcome of the alteration. Metastable phases, which are rapidly converted into more stable minerals in warm and wet climates, could be preserved in colder conditions, and concentrate during weathering (Bender Koch et al., 1995).

Antarctic basaltic samples have become naturally appealing as analogues of alteration in the present-day cold and dry Martian environment (Allen and Conga, 1991). Previous studies on Antarctic basaltic material showed the formation of minor clays and iron (oxy)-hydroxides resulting from weathering by thin layers of liquid water (Dickinson and Rosen, 2003). For example, Chevrier et al. (2006a) demonstrated that alteration in dry and cold climate for up to 10 Myr remained very limited. Their study also showed that alteration products were dominated by metastable maghemite which progressively transformed into hematite, providing a simple pathway for the coexistence of strongly magnetic and colored nanophases in the Martian regolith. Other studies using multiple mineralogical, chemical and spectral analyses (Salvatore et al., 2013, 2019) demonstrated that mineralogical changes using XRD remained very limited, especially for basaltic rocks, while spectral properties significantly changed between altered surfaces and fresh samples. In the present study, we propose to pursue the analysis of a single continuous weathering profile of the Antarctic Ferrar dolerite by focusing on the mineralogy and chemical composition, using different analytical techniques, as well as spectral properties. The aim is to identify the weathering products encountered on the Martian surface, as well as to improve the knowledge of the conditions in which the Martian surface was altered.

2. Materials and methods

2.1. Sample description and preparation

The Ferrar dolerite sample presented in this study (Fig. 1A) was collected specifically for rock varnish study by A. Meloni (INGV Roma) about 20 years ago during a PNRA expedition on the northern side of the Priestley Glacier, Antarctica (Lat: 74°S, Long: 163°E, altitude around 3000 m above sea level) and has been described by Chevrier et al. (2006a). In this area, the Ferrar dolerite outcrops on top of the granitic basement just above the ice sheet. Thus, they have been exposed at the surface without disturbances for a very long time. Exact sampling conditions are not known, but being conducted during rapid helicopter surveys, it is very likely that a top mountain flat crest was chosen. The subsequent experiences of one of the co-authors (P. Rochette) during three PNRA expeditions on Ferrar dolerite bearing nunataks of this area (e.g. Merchel et al., 2010) or in the Dry Valleys, revealed similar looking weathering crusts on Ferrar dolerite samples. Exposure ages measured on such surfaces are of the order of 1 Myr or more (Folco et al., 2008, 2016; Schäfer et al., 1999). Based on the altitude and sampling setting, the weathering of the rock surface must have occurred either on contact with the atmosphere or with temporary snow cover. Air temperature above the ground is always much below zero (at most about −20 °C), and contact with liquid water may have been exceptional. This situation may have occurred only when the sun heats a dark rock surface, reaching positive temperatures, and melting a thin snow cover. Note that the dolerite block was showing a single well-developed weathering varnish side that was likely the most exposed surface (i.e. exposed to the sun).

The Ferrar dolerite presents geochemical and mineralogical similarities with Martian igneous rocks (Bandfield et al., 2000), despite being more silica-rich than averaged Martian basalts. This similarity of modal mineralogy makes these andesitic basalts interesting to study possible alteration processes in the present-day Martian climate. The petrologic study of this sample shows that it is a fine grained tholeiitic to andesitic basalt composed of 55–60% of randomly oriented laths of feldspars (plagioclase), 15–20% of both coarse ortho- and clinopyroxene and <5% of Fe and Ti oxides, cemented by a 20–25% dark glassy or

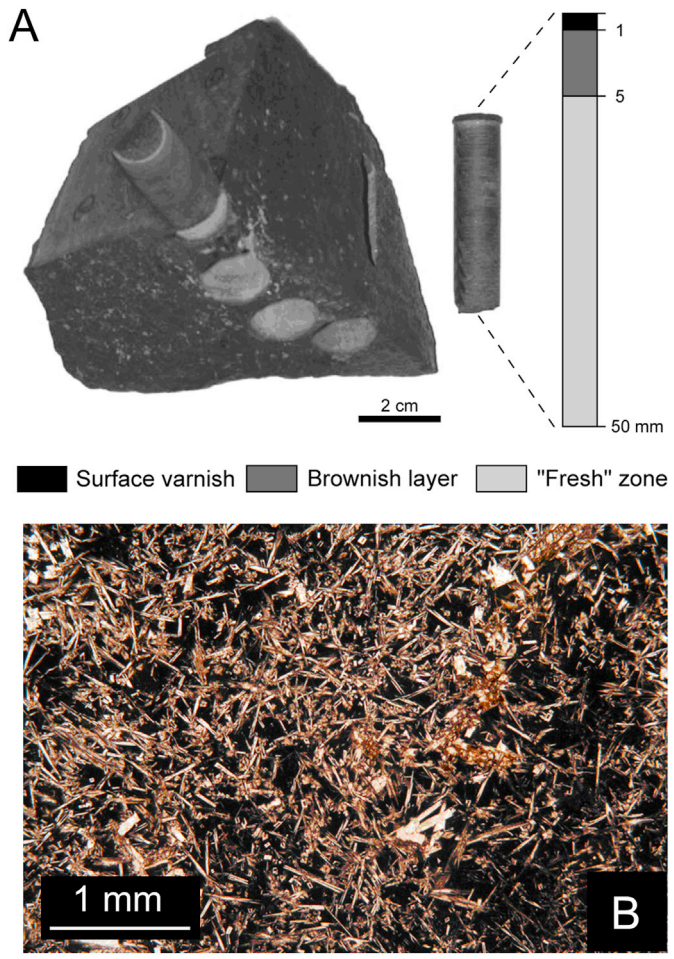

Fig. 1. A) Ferrar dolerite macroscopic sample showing the brownish surface rind and the fresh core. As shown by the sketch of the apparent structure of the weathering profile, samples characterized by XRD, SEM and infrared spectroscopy were extracted from the drill core cylinder at different depths. B) Plane-polarized light (PPL) image showing the texture and rock-forming minerals of the Ferrar dolerite sample.

microcrystalline matrix (Fig. 1B, Gunn, 1962). The weathered surface is characterized by a 1 mm-thick brownish surface rind (Fig. 1A), followed by a discolored zone down to about 5 mm deep and then the apparently dark fresh core. The original drill core (1 cm in diameter) prepared in our previous mineralogical and magnetic characterization has been used for this study (Fig. 1A, Chevrier et al., 2006a). The drill core had been previously sliced in order to get materials representative of different depths (i.e. 0 to 1, 1 to 3, 5, 9, 13, 17, 21, 25, 29 and 33 mm), allowing the analysis of the alteration profile from the surface rind to the fresh rock core. Following our previous study, all the slices were crushed to a grain size of ~200 μm. In addition, the surface rind was sampled separately by abrading approximately 0.5 mm of materials using a Dremel drill tool. The original thin section which was prepared along the drill core for microscopic observations was also used (Fig. 1B). A rough section of the sample (~5 cm in diameter) was prepared to be scanned with a hyperspectral (HySpex) camera. Thus, all profiles and results presented by this study can be directly compared to the results obtained by Chevrier et al. (2006a).

2.2. Sample characterization

2.2.1. X-Ray Diffraction analyses

The X-Ray Diffraction (XRD) analyses of the fresh rock core and the weathered rind (<0.5 mm thick) were performed with a Philips PW 3710

θ/2θ diffractometer using a $Co_{K\alpha}$ (k = 1.79 Å) radiation with a secondary flat graphite monochromator. The diffractometer optics used to analyse all samples was a front fixed slit of 1°, a scattered-radiation slit of 1° after the sample and a detector slit of 0.2 mm. The X-ray tube operating conditions were 35 kV and 30 mA. The 2θ range was 5–80° in 0.02° steps and a counting time of 13 s per step, resulting in a total counting time of 13 h and 45 min per sample. All powder samples were spread on a crystallographically oriented silicon plate (no Bragg peaks) and homogenized with alcohol to obtain a thin and homogeneous layer. 50 wt% of finely powdered quartz were added to both core and surface rind samples in order to calibrate the spectra and control any possible instrument drift. Therefore, the presence of quartz in the XRD patterns is not related to the mineralogical composition of the Ferrar dolerite and can't be used for mineralogical characterization of the wathering profile.

2.2.2. Scanning Electron Microscopy analyses

Scanning Electron Microscopy (SEM) observations were completed using a Philips XL 30 ESEM (Saint Charles Faculty, Marseille, France) coupled with an EDX analytical system (EDAX) for semi-quantitative chemical analyses. This system allowed the generation of elementary maps showing the spatial distribution of elements over a zone of 1.2 mm width and 6.7 mm length along the thin section. Eight images, acquired along the weathering profile, were stitched together to generate a mosaic image or elementary map. A counting time of 30 s was used to analyse each element (e.g. Si, Al, Fe, Mg, Ca, Na, Cl). Additional observations were performed using a JEOL JSM-6320F (CRMCN, University of Aix-Marseille III, Luminy, Marseille, France) with an accelerating tension of 15 kV.

2.2.3. Laser-Induced Breakdown Spectroscopy analyses

Chemical analyses were obtained with a Laser-Induced Breakdown Spectroscopy (LIBS) technique at the IRAP (Toulouse, France), using a replica - the Engineering Qualification Model (EQM) - of the ChemCam instrument that is currently onboard the Curiosity rover (Maurice et al., 2012; Wiens et al., 2012). An optical system is used to focus a 1067 nm Nd:KGW pulsed laser on the target (with an energy on target of 10 mJ and a pulse width of 5 ns), which produces a short-lived plasma with atoms or ions in an excited state. Each laser pulse produces a spectrum of emission lines, which, in our case, is integrated over 3 ms and recorded over three spectral ranges: 240–342 nm, 382–469 nm and 474–907 nm. Spectral analysis of the atomic or ionic emissions lines allows identifying elements present in the sample as major elements (e.g. O, Si, Fe, Na, K, Mg, Al and Ca) and a large series of minor and trace elements (such as H, Ti, Mn, Li, C, N, F, P, S, Cl, Cr, Ni, Cu, Zn, Sr, Rb, etc.).

Two series of 600 laser pulses (i.e. 600 spectra) were acquired at two locations on the edge of the dolerite section, from the fresh surface to the core of the sample, to obtain chemical depth profiles. Over this range of shot number, each laser shot typically ablates ~0.3 μm of sample material in basaltic rocks (Cousin, 2012). The spatial scale of the analysis is ~425 μm (Chide et al., 2019). The analyses were performed under a ~7 mbar CO_2 atmosphere, which is representative of Martian conditions, but also optimal for LIBS measurements (Cousin et al., 2011; Effenberger and Scott, 2010; Sallé et al., 2006) except to measure carbon and oxygen (Dequaire et al., 2017). This technique used with ChemCam's EQM under representative Martian conditions has the potential to provide a direct basis of comparison between laboratory data and possible Mars observations done by ChemCam.

Absolute elemental quantification of diverse geological samples using LIBS requires the use of a large calibration set of standard samples. Nevertheless, relative analyses of elemental abundances are much simpler to obtain, using either univariate or multivariate analytical techniques. Multivariate analyses take advantage of the large spectral range by considering that the observed spectra are linear combinations of pure element sources and that the simultaneous analysis of several emission peaks gives a better statistical sampling of the proportion of a given element compared to the analysis of individual peaks. In this study, the chemical variations in depth are investigated using an Independent Component Analysis (ICA) technique (Forni et al., 2013), which is a multivariate statistical and computational technique for revealing hidden factors that underlie sets of random variables, measurements, or signals (Comon, 1994; Hyvärinen et al., 2001). Each spectrum was decomposed into 10 components (or spectra) that are mutually independent from each other and which were derived from the analysis of the ChemCam Martian dataset (Clegg et al., 2017). These components happen to be dominated by emission lines from different elements (Si, Ti, Al, Fe, Mg, Ca, Na, K, H and Li in the case of the present study). The weight or contribution of each component to each measured spectra, hereafter called "ICA score", is computed by calculating the correlation coefficient between both. The ICA scores vary monotonically with abundance (Clegg et al., 2017). Comparing the ICA scores provides a way to analyse chemical variations that are closely tied to the information contained in the spectra (as can be seen by comparing spectral regions in Fig. 5 with ICA scores in Figs. 6 and 7), albeit not in an absolute quantitative way.

2.2.4. Infrared spectroscopy

2.2.4.1. Powder sample spectra. The reflectance spectra of the powder samples collected at different depths were measured at the LPG Nantes (University of Nantes, Nantes, France) using a Nicolet 5700 FT-IR spectrometer (Thermo Nicolet Corporation, USA). The spectral readings were performed using a Smart Diffuse Reflectance accessory at room conditions (T ≈ 20 °C and P ≈ 10^5 Pa). An Infragold reflectance standard was used to derive the absolute reflectance of each sample. A quartz-halogen source was employed for two beam-splitter/detector configurations to obtain spectra in two different spectral ranges. The quartz/silicon configuration covered the 0.70–1.10 μm wavelength range (i.e. ~15,000–9000 cm^{-1}) while the CaF_2/DTGS (Deuterated Triglycine Sulfate) configuration acquires spectra from 1.00 to 4.70 μm range (i.e. ~10,000–2100 cm^{-1}). The spectral acquisitions were set to measure the average of 100 and 200 stacks respectively. Spectra acquired in those two different spectral domains were stitched together by using the silicon detector as a stable reference and finding a linear relation in the overlapping spectral range (i.e. from 1.00 to 1.10 μm). The measurements were done with a spectral resolution of 4 cm^{-1}. Each spectrum was then resampled at a resolution of 3.5 nm in order to have a uniform sampling interval in wavelength and to reduce the noise.

The shifts in wavelength of key absorption bands as well as the variations of both the absorption band-depth and/or the band-area can be computed in order to quantitatively estimate the compositional mineralogical changes on a sample (Chevrier et al., 2006b; Clark and Roush, 1984; Nolin and Dozier, 2000). Two spectral parameters have been defined to analyse the sample spectra at three different wavelengths ranges (see Table 1). The analysis of the ~1.00 and ~2.00 μm bands diagnostic of the iron present in pyroxenes (Hunt and Salisbury, 1970) was done using the 0.75–1.20 μm and the 1.60–2.60 μm spectral range respectively. Note that the absorption band of the ferric iron of (oxy)-hydroxides occurring near 1.00 μm overlap the pyroxene features and can also be analysed using this same spectral parameter. The hydration band, occurring at 2.80 μm, was studied within the 2.60–4.00 μm spectral range. Spectra have been continuum removed using the technique proposed by Clark and Roush (1984) to enhance the differences in shape and

Table 1
Wavelength ranges used to remove the continuum and to study the evolution of the clinopyroxene and the plagioclase absorption bands as well as the hydration bands.

Continuum removal intervals (μm)	Analysed spectral processes
0.75–1.20	Evolution of the 1.00 and 2.00 μm clinopyroxene bands
1.60–2.60	
2.60–4.00	Evolution of the 2.80 μm hydration band

to isolate the absorption features. The depth of an absorption feature D is defined relative to the continuum ρ_c by the following equation:

$$D = \frac{\rho_c - \rho_b}{\rho_c} \quad (1)$$

where ρ_b is the reflectance at the band bottom and ρ_c is the reflectance of the continuum at the same wavelength λ (Clark and Roush, 1984). The position in wavelength for an absorption feature is defined by the wavelength where the reflectance is minimal after the continuum removal. The integrated band area of an absorption feature (S_{abs}) is obtained by adding the reflectances over the spectral range (d_λ) that defines the considered absorption feature after continuum removal (Nolin and Dozier, 2000) as follows:

$$S_{abs} = \sum_{\lambda=b_{\min}}^{b_{\max}} (1 - \rho_\lambda) \cdot d_\lambda \quad (2)$$

2.2.4.2. Hyperspectral image of the sample. The Ferrar dolerite sample was scanned using three HySpex hyperspectral cameras (LPG Nantes, University of Nantes, Nantes, France). The Vis-NIR range was covered with a VNIR-1600 camera equipped with a Silicon CCD detector array. This device acquires a full spectrum with a spectral sampling interval of 3.7 nm between 0.40 and 1.00 μm in 160 bands. Two cameras were used to cover the SWIR. The SWIR-320i covers the wavelength range from 0.90 to 1.70 μm in 147 bands with an InGaAs (indium-gallium-arsenide) detector while the SWIR-320m camera is equipped with an HgCdTe (mercury-cadmium-telluride) detector array that measures the light

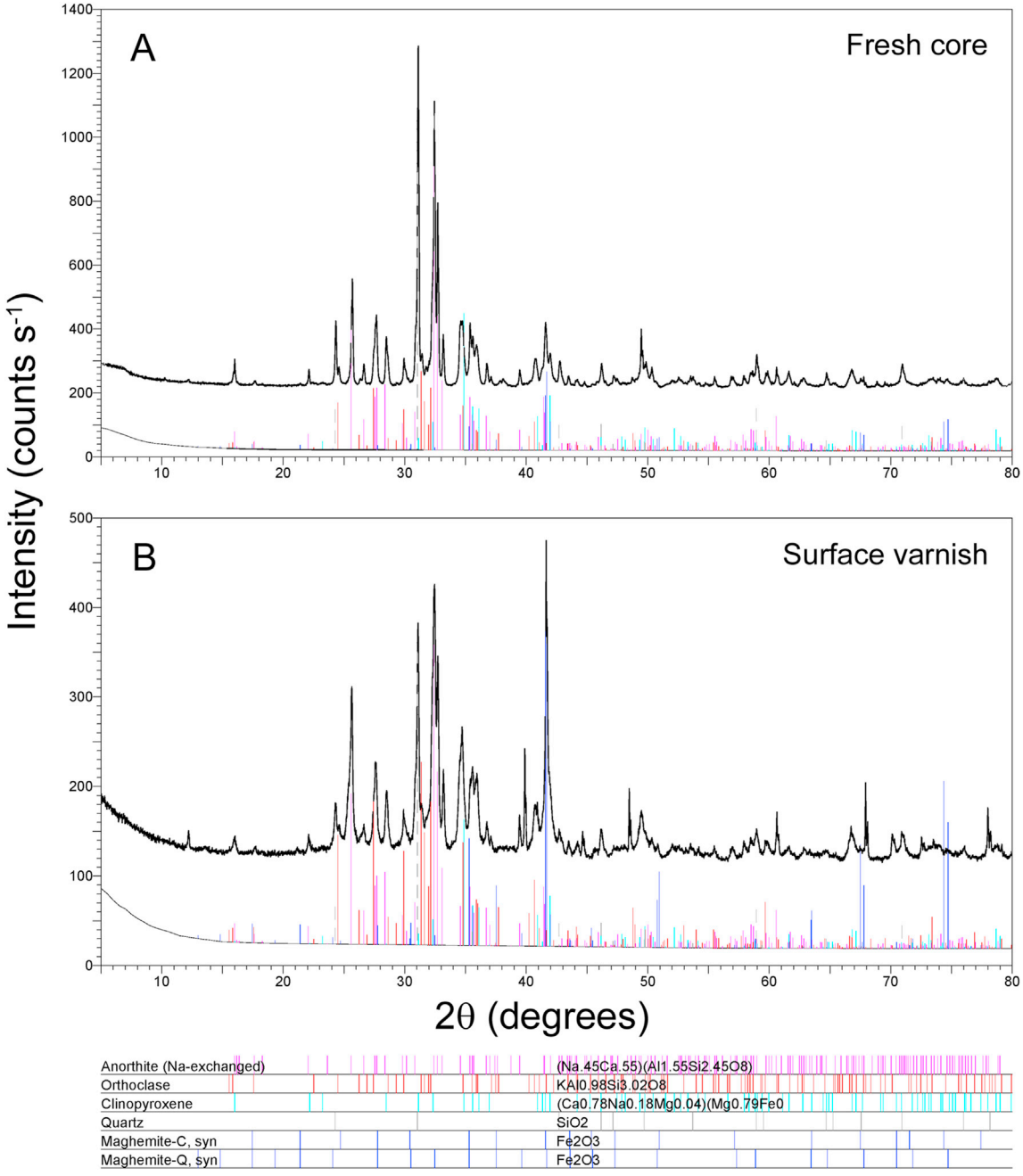

Fig. 2. XRD spectra of: A) the surface rind (<0.5 mm thick) and B) the fresh rock core of the Ferrar dolerite. The patterns used for the identification of the mineral phases are presented in the bottom. Note that quartz is a minor constituent of the Ferrar dolerite and was artificially added to the sample preparation to calibrate the position of the peaks.

between 1.30 and 2.50 μm in 239 bands. Both SWIR cameras have a spectral resolution of 5 nm. The distance between the cameras and the sample is 30 cm. The scanning speed is synchronized to the speed of the spectral acquisition of each line to achieve a final image with a spatial resolution of about 0.2 mm/pixel with the Vis-NIR camera and 0.85 mm/pixel for both SWIR cameras.

The laboratory measurements were done using a halogen lamp giving energy up to 2.50 μm. A white standard panel made of Spectralon® was used in the scene as a reference material to convert the obtained spectral data into reflectance data. Spectral correction was done in two steps: i) a radiometric correction of photon counts in radiances, including factory calibration between columns for each hyperspectral cameras separately, and ii) a reflectance conversion which is given in the scan direction by dividing each pixel by the mean of the Spectralon® digitized spectrum present in each image and multiplied by the Spectralon® factory spectra. The spectral domains covered by the three cameras were merged using the CCD detector as a stable reference and finding a linear relation in the overlapping spectral range (i.e. from 0.90 to 1.00 μm and from 1.60 to 1.70 μm). For this process, the Vis-NIR hyperspectral image was resampled to the spatial resolution provided by the SWIR cameras. Two color composites images were defined and two band ratios were calculated from the hyperspectral data cube to highlight the mineralogical variations as well as to map spectral heterogeneities of the sample from the sample surface rind to the fresh zone.

3. Results and mineralogical interpretations

3.1. Mineralogy and chemistry

The analysis of the XRD patterns for the fresh core and the weathered rind shows significant differences. The fresh core sample has a relatively simple composition, largely dominated by anorthite, with clinopyroxene and minor orthoclase (Fig. 2). The weathered sample shows a similar composition; however, the maximum intensity is much lower (i.e. ~480 counts s^{-1}, see Fig. 2A) than the one observed for the fresh sample (i.e. ~1300 counts s^{-1}, see Fig. 2B). This is mainly due to the decrease in intensity of the anorthite, while the two other phases present similar intensities in both samples. Despite its likely presence in the sample (Elliot et al., 1995), characterizing the presence of quartz was not possible due to its use as a control for peak position. However, previous analyses have shown that quartz should account for ~5% of the mineral modal abundance in the dolerite (Zavala et al., 2011). The other significant feature in the weathered sample is the presence of a major peak at $2\theta = 42°$, and a second peak or lower intensity at $2\theta = 68°$ (Fig. 2A). The peak at $2\theta = 42°$ is also present in the fresh sample, albeit with a lower intensity. These peaks are best matched by maghemite γ-Fe_2O_3, although the two spectra, labelled maghemite-C and maghemite-Q, present a significant peak at $2\theta = 74.5°$ that is not observed in the weathered sample. Therefore, a specific form of maghemite may be present, which appears to be the only phase to fit the 42° peak and still be consistent with the overall chemistry of the sample. Finally, a single peak observed at $2\theta = 12°$ probably indicates the presence of smectite at the surface of the sample. It is interesting to note that this peak is virtually absent in the core of the sample.

The XRD results are confirmed by the chemical mapping along the weathering profile. The Si, (Al + Ca) and Mg elemental maps clearly identify the three major phases in which these elements are concentrated: amorphous glass, feldspars and pyroxenes, respectively (Fig. 3). Sodium appears relatively homogeneous, except in the pyroxenes, where it is depleted. Iron is an element of major importance when studying aqueous alteration or weathering, because its oxidation state changes between Fe^{II} and Fe^{III} resulting in various minerals that reflect the environmental conditions. Chevrier et al. (2006a) observed an enrichment in iron towards the surface using bulk chemical analyses. The Fe elementary map shows a very clear depletion where Al is concentrated (i.e. in the plagioclase). Alternatively, Fe is slightly concentrated in the mineral

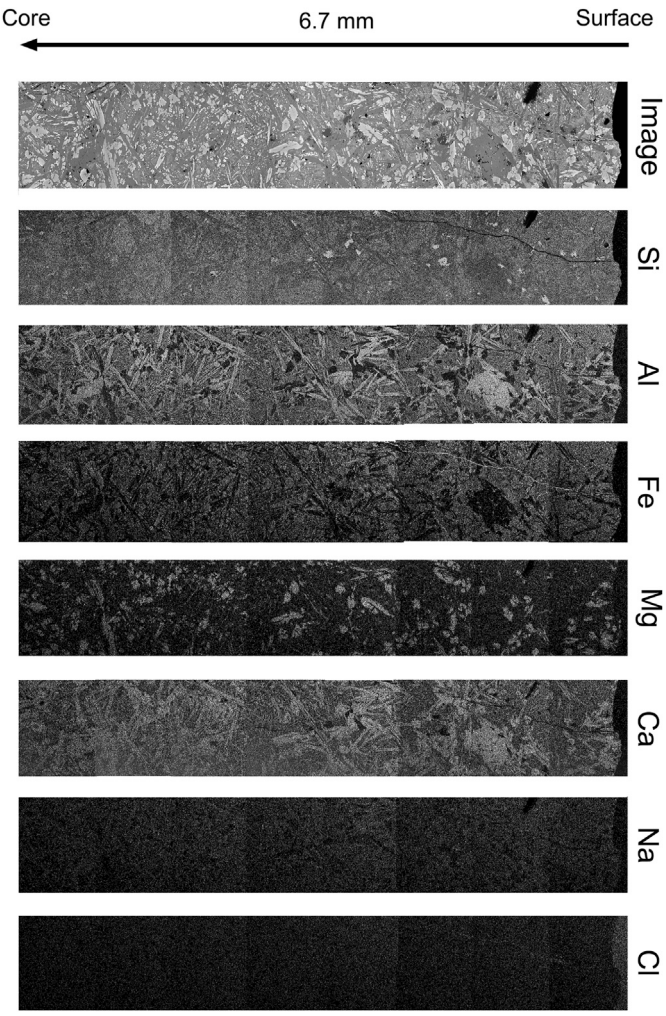

Fig. 3. Image and elementary maps of the weathering profile, determined using a SEM coupled with an EDAX. Each map is the result of the combination of eight individual pictures, stitched to each other. From top to bottom: SEM image, Si, Al, Fe, Mg, Ca, Na, and Cl maps.

phases where Mg is present (i.e. pyroxenes). Note that Fe does not seem to concentrate on the very top surface of the profile (Fig. 3). This suggests the absence of a surface varnish or a coating that it is too thin to be observed at the resolution of the ESEM (Campbell and Claridge, 1987; Cannon et al., 2015; Salvatore et al., 2013). The last and most interesting observation is the presence of a thin vein connected to the surface that shows a strong enrichment in Fe, but also a depletion in Si and a slight enrichment in Cl (Fig. 3). The chemical composition of this vein indicates that it most probably results from weathering. The presence of chlorine is typical of marine aerosol contribution that is commonly observed in Antarctic surfaces even far from the ocean (here distant from the outcrop by about 80 km). Chloride crystals have also been previously observed on the surface of the sample (Chevrier et al., 2006a).

The ESEM analysis of the vein exhibits a plasma structure and concentric accumulations within its interior (Fig. 4). Elemental analysis of the accumulated product indicates the presence of iron with minor manganese (Table 2, shots number 1, 3 and 4). Therefore, the products filling the vein are interpreted as being an iron (oxy)-hydroxide. However, there is no certitude that this phase is equivalent to the maghemite identified in the XRD spectra and by the previous magnetic analyses (Chevrier et al., 2006a). The morphology rather suggests nanophase iron (oxy)hydroxides. But this is very distinct from the well-defined crystals of primary inherited titanomagnetite (Fig. 4, Table 2, shot number 6).

The LIBS depth profiles exhibit various relative correlations between

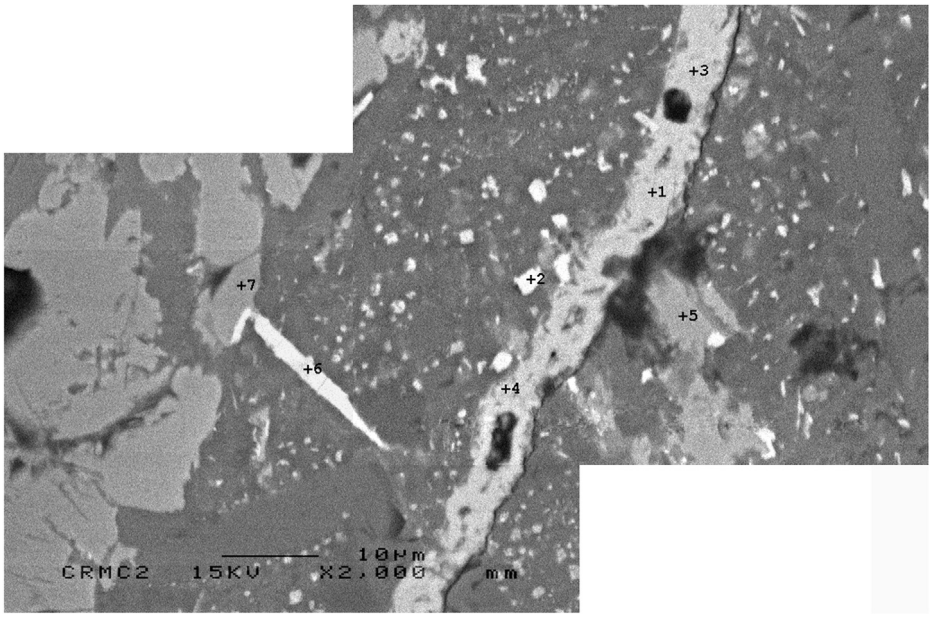

Fig. 4. SEM picture of the Ferrar dolerite (mosaic done using two images) showing the vein identified on the chemical maps (see Fig. 3). The vein is filled with iron (oxy)-hydroxides showing plasma structure. The bright crystals are iron sulphides. The crosses and numbers indicate EDAX individual analyses (shown in Table 2).

Table 2
EDAX analyses of various minerals in the Ferrar dolerite sample (points shown on Fig. 4).

Shot #	1	2	3	4	5	6	7
Wt%							
S	1.4	0	2.8	0.99	N.A.#	0	N.A.#
Ti	0.94	5.34	0	0		44.38	
Cr	0	0	0	0		0	
Mn	0.7	0	1.8	1.18		1.66	
Fe	95.64	93.8	94.84	93.2		53.36	
Co	0	0	0	0		0	
Ni	0	0	0	2.83		0	
Al	1.32	0.86	0.56	1.81		0.6	
Total	100	100	100	100.01		100	
At%							
S	2.38	0	4.75	1.68		0	
Ti	1.06	6.12	0	0		47.9	
Cr	0	0	0	0		0	
Mn	0.7	0	1.79	1.17		1.56	
Fe	93.2	92.13	92.34	90.88		49.39	
Co	0	0	0	0		0	
Ni	0	0	0	2.62		0	
Al	2.66	1.75	1.12	3.66		1.15	

#Only qualitative spectra were acquired and showing pyroxene composition.

elemental peak intensities. There is a strong positive correlation between Si and Al (Figs. 5 and 6A), Na (Fig. 6B) and K (Fig. 5, Fig. 6C). Note that the second depth profile is not shown but gives similar results. These results suggest the presence of feldspar in the measured samples. Moreover, the surface data (i.e. colored points on Fig. 6, corresponding to the first shots of the depth profile) align on the same trend as the deeper measurements (i.e. black points on Fig. 6). This indicates that the composition of the feldspar does not significantly change in the altered front, although the surface measurements are slightly enriched in Na and K, while depleted in Al. The fact that Al is not exactly aligned with the rest of the data suggests incongruent dissolution of feldspar, possibly accompanied by a migration of Na and K to the surface (Cannon et al., 2015; Salvatore et al., 2013). Moreover, LIBS measurements exhibit a strong anticorrelation between Si, Mg (Figs. 5 and 6D) and Ca (Figs. 5 and 6E). Such results indicate that Ca and Mg are carried by a phase that is Si-poor and mixed with the Si-rich phase (itself correlated to Al), and therefore that Ca and Mg are probably carried by mafic minerals, most likely pyroxenes. Therefore, the overall signal shows mixing of mafic and alkaline silicate phases, combining enrichment in feldspar and depletion in pyroxene towards the surface of the sample at the ~400 µm scale of the LIBS depth profile.

Iron shows a more complex behaviour. There is a significant increase of Fe towards the surface (Figs. 5 and 6F), combined with an increase of hydrogen (Fig. 7A). This is particularly visible when comparing the individual signals for Fe and H as a function of shot number (Fig. 8A and B). Fe and H are particularly enriched in the first 30–40 shots, as well as deeper (i.e. around 150–200 shots). The deeper shots have most likely sampled the edges of the LIBS crater, and thus the fresh surface as well (probably due to a small jitter of the laser beam in between each burst of 150 shots). This strong correlation between Fe and H (Fig. 7A) suggests the presence of iron (oxy)-hydroxides close to the surface of the sample. Therefore, the positive correlation between Fe and Si (Fig. 6F) is probably the result of enrichment in feldspar and iron (oxy)-hydroxides near the sample surface. On the other side, in the deeper shots, hydrogen becomes independent from iron, suggesting the signal from iron (oxy)-hydroxides become negligible. Finally, the strong correlation observed between Fe and Ti (Figs. 5 and 6B) suggests that iron is partly carried by Fe–Ti-rich phases, most probably titanomagnetite or its oxidized counterpart titanomaghmemite (Chevrier et al., 2006a).

Another significant element in the weathering profiles is manganese. LIBS measurements do not show any clear correlation between Mn and Fe (Fig. 7C), although Mn is slightly decreasing from the surface to the core (Fig. 8C). This demonstrates that although Mn is affected by surface weathering, it is not concentrated in iron (oxy)-hydroxides.

Fluorine is also detected at the surface of the sample (Fig. 9), through the emission of a CaF molecular band at ~603 nm, resulting from the recombination of Ca and F in the plasma. Particulate fluorides usually include cryolite (Na_3AlF_6), chiolite ($Na_5Al_3F_{14}$), calcium fluoride, aluminum fluoride and sodium fluoride (Lewandowska et al., 2013). The lack of Al or Ca enrichment (Fig. 6A, E) and the increase of Na in the first shots of the depth profile (Fig. 6B) suggests the presence of sodium fluoride. Correlation between F and Na was used to point out a contribution of fluoride from sea salt in precipitation samples collected from marine, coastal and inland sites in India (Mahadevan et al., 1986).

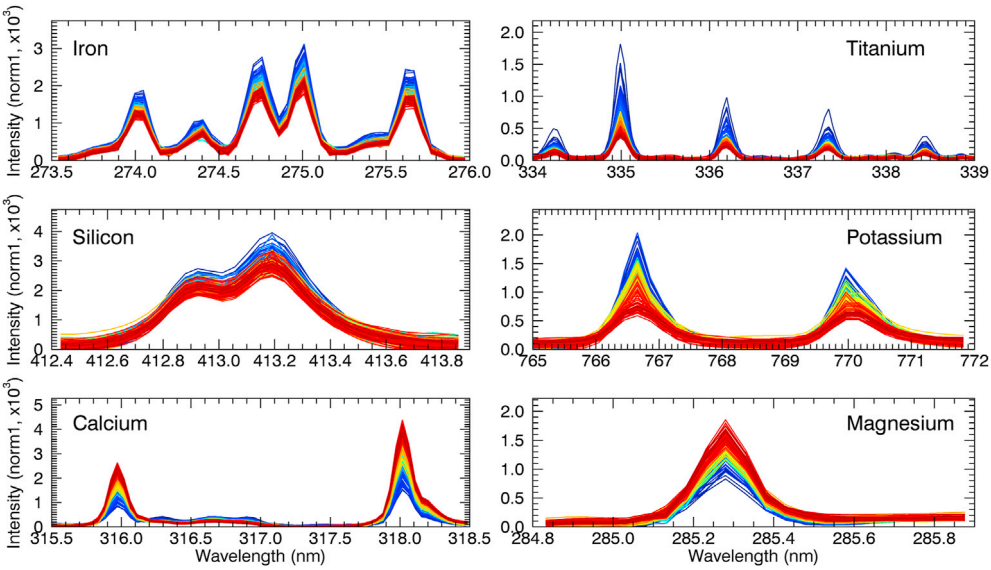

Fig. 5. Shot-to-shot LIBS spectra (150 shots, second burst) of the depth profile (with increasing shot number from blue to red), over several spectral regions of interest. The Bremsstrahlung-continuum has been removed and the spectra have been normalized by their total intensity (after continuum removal) to correct for possible variations of laser coupling with depth, although the total intensity has not been observed to vary significantly with shot number (see Fig. 8D). The Bremsstrahlung continuum, on the other hand, was observed to increase with depth, possibly due to increased plasma shielding and transfer of energy to free electrons. (For interpretation of the references to color in this figure legend, the reader is referred to the Web version of this article.)

3.2. Reflectance spectroscopy and hyperspectral imagery

The VIS-NIR reflectance spectra of the samples corresponding to the depths 1, 3, 5, 9, 13, 17, 21, 25, 29 and 33 mm are shown in Fig. 10. Several characteristic absorption features dominate the spectra. A deep absorption band centred at 1.00 μm is present and seems to be correlated to another one between 2.10 and 2.20 μm. Both absorptions are diagnostic of ferrous iron in clinopyroxene (Hunt and Salisbury, 1970). The exact position in wavelength of the 1.00 μm and 2.10–2.20 bands suggest the presence of augite as the dominant clinopyroxene endmember (Fig. 11). A very strong and round shaped feature at 2.80 μm indicates the presence of adsorbed and structural water in the samples (Milliken and Mustard, 2007a, b; Pommerol and Schmitt, 2008). Finally, two very shallow absorption bands at 3.41 and 3.50 μm appear in the spectra (Fig. 10). These two shallow bands are most likely related to contaminants originating from organic material from the sampling site (proximity to the ocean) or from compounds used during sample handling and preparation prior to analysis.

The surface rind is clearly visible on the color composite image that covers the visible range of the hyperspectral image (Fig. 12A). The rind penetration is around 1–2 mm, followed by a discoloration zone that penetrates down to about 5–10 mm and it is characterized by a lighter color than the fresh core that appears greenish grey. The footprint of the surface rind is even more evident on the Vis-NIR color composite (Fig. 12B). The oxidized rind appears blue-green, the transition zone shows orange-yellow colors and the fresh core is dark brown.

The spectral profile derived from the hyperspectral image of the macroscopic sample (Fig. 13) shows a similar behaviour to the spectra collected on the powder samples (Fig. 10). However, the amplitude of the absorption bands at 1.00 and 2.00 μm and that of the shoulder at 0.75 μm are much more attenuated than those observed on the powder spectra. These differences are related to the surface state created by the sample preparation methods (i.e. powder v/s sawn surface). The spectral response obtained with the hyperspectral camera in the Vis-NIR shows a truncated band near 0.51 μm and 0.95 μm (Fig. 13). Both features are stronger near the sample surface and tend to disappear towards the fresh core. Both phenomena can be characterized by calculating the ratio between the band shoulders (750 nm) and the band centre (510 and 950 nm). Therefore, the ratio R950/R750, shown in Fig. 12C, highlights the discoloration zone (darker indicates deeper 950 nm band) while the ratio R750/R510, displayed in Fig. 12D, characterize the surface rind and associated veins (darker indicates deeper 510 nm band).

Although all spectra from the fresh rock core to the surface rind appear relatively similar at first sight (Figs. 10 and 13), they exhibit subtle variations of the spectral properties with depth, probably related to the weathering gradient previously characterized in this core (Chevrier et al., 2006a). Previous mineralogical observations showed the formation of iron (oxy)-hydroxides towards the surface. Two possible candidates have been identified: maghemite and hematite, the former being metastable with respect to the latter (Chevrier et al., 2006a). The maghemite spectrum shows an overall flat response in the Visible Near-Infrared (Vis-NIR) region (from 0.80 to 2.60 μm in Fig. 11). However, this mineral could be responsible for the change in shape of the spectra near 1.10 μm and 2.50 μm (Figs. 10 and 13). The spectral response of maghemite could also explain the attenuation of the maximum of reflectance of clinopyroxene near 1.60 μm, the disappearance of the 2.00 μm feature, and the smoothness of the 2.75 μm band of augite (as shown in Fig. 11), especially for surface samples. Moreover, a more pronounced rounded shape of the 2.80 μm band towards the surface could also be related to the presence of maghemite.

3.2.1. Spectral evolution of the 1.00 and 2.00 μm range

Fig. 14 presents the evolution of the 1.00 and 2.00 μm continuum removed bands between two intervals: 0.75–1.20 μm (Figs. 14A) and 1.60–2.60 μm (Fig. 14B) respectively. Although the first absorption band is centred at 1.00 μm, the 2.00 μm-band is centred at 2.15 μm (Fig. 14B), suggesting a mixture of clinopyroxene with a small amount of orthopyroxene (Adams and McCord, 1972).

The band area parameters shown by Fig. 14C, which correlates the 1.00 μm versus the 2.00 μm band areas, will be discussed in the following sections. Fig. 14C shows that there is a clear correlation between the 1.00 and 2.00 μm bands area in all the samples and indicates that a significant component of pyroxene is present (Fig. 11). The fresh core samples are characterized by lower values of 1.00 μm and 2.00 μm bands, which increase towards the discolored zone. The maximum values are for 3 and 5 mm deep samples. The 1 mm deep sample occupies an intermediate position. Both pyroxene bands do not correlate with the overall spectral albedo (the average albedo is 0.09 and values range from 0.08 to 0.12). This lack of trend demonstrates that the spectral parameters used in this study and compared to other chemical analyses are not artefacts.

The evolution of both the 1.00 μm and the 2.00 μm band area with depth has been compared to the chemical profiles for various major elements (e.g. FeO, MnO, MgO, CaO and SiO_2 in Fig. 15) that were previously measured by Chevrier et al. (2006a). Except for the 1 mm deep sample, the evolution of the 1.00 μm and 2.00 μm bands area is positively correlated with the MnO and FeO contents (Fig. 15A), suggesting an

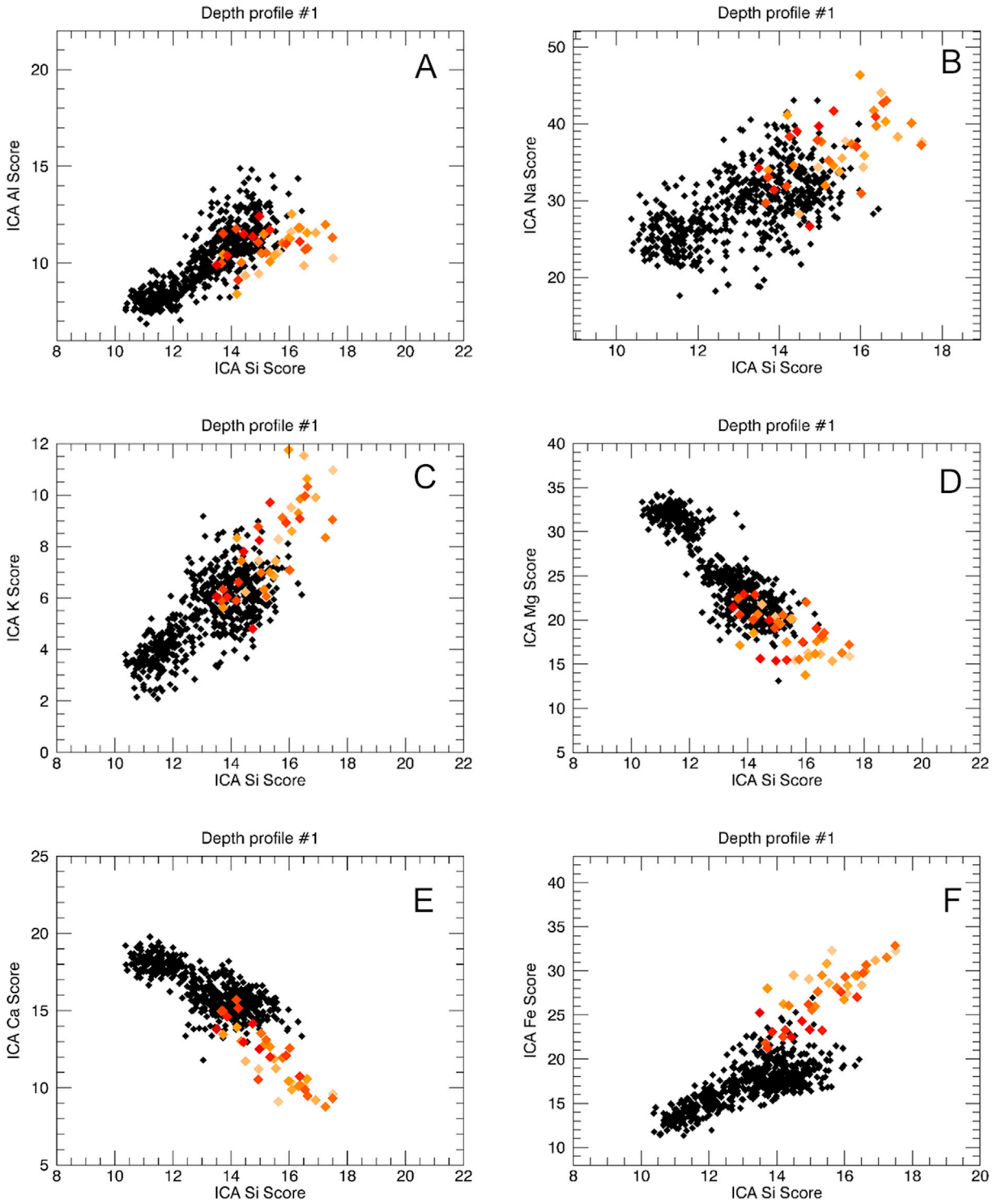

Fig. 6. LIBS measurements of Ferrar dolerite. Depth profile ICA score plot: A) Si v/s Al, B) Na, C) K, D) Mg, E) Ca and F) Fe. Points colored in brown tones were measured near the surface while the black points correspond to the measurements done deeper in the sample. (For interpretation of the references to color in this figure legend, the reader is referred to the Web version of this article.)

increase in pyroxene abundance in the discolored zone.

3.2.2. *Evolution of the 2.80 μm hydration band*

Fig. 16A shows the continuum removed spectra of samples between 2.60 and 4.00 μm, emphasizing the 2.80 μm hydration feature. The depth and width of this feature decrease from the surface to the inner fresh core, indicating a stronger hydration of the surface materials. Fig. 16B compares the 2.80 μm band area evolution with depth to the H_2O content (after heating the samples to 110 °C) and Lost On Ignition (LOI, volatiles lost at about 900 °C) as measured by Chevrier et al. (2006a). There is a moderate to strong correlation between the band area and the LOI (Fig. 16C). The correlation with H_2O is weaker and mostly limited to the increase close to the surface, related to increased hydration in the more porous surface (e.g. presence of veins as in seen in the element maps, see Figs. 3 and 4).

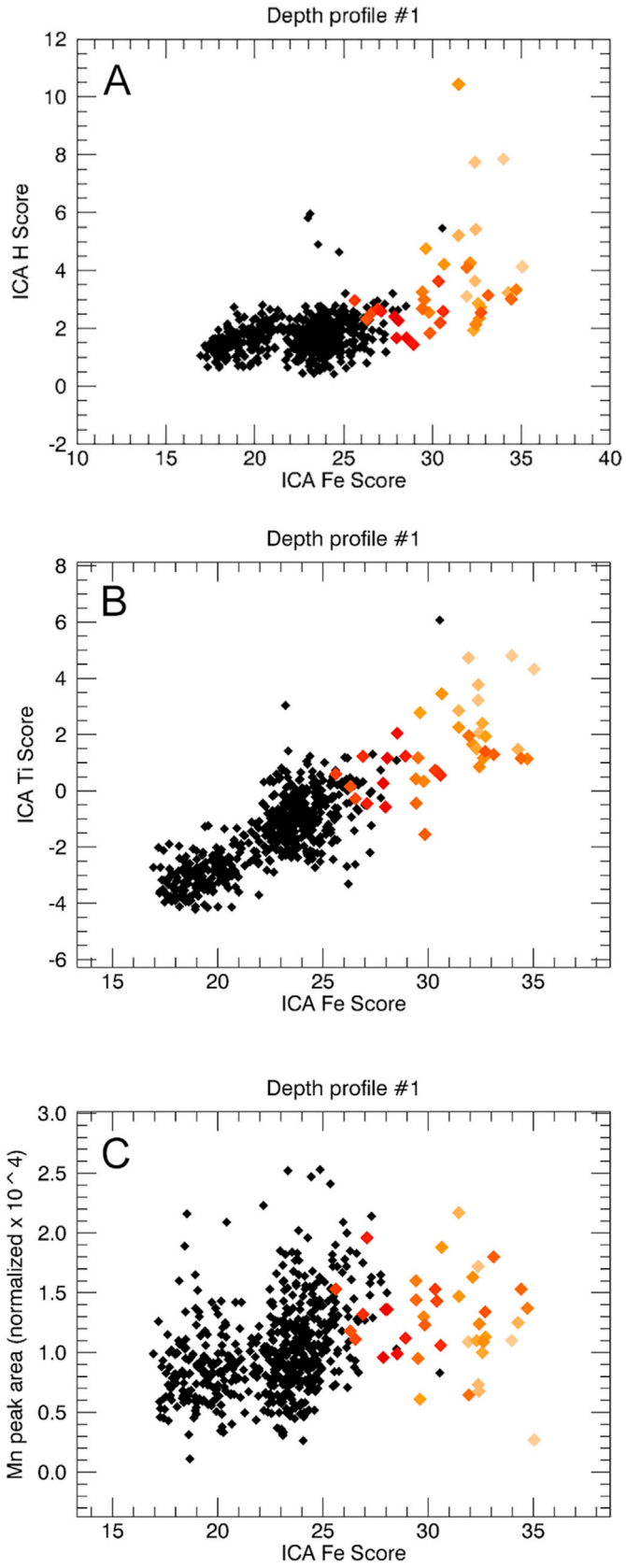

Fig. 7. Depth profile ICA score plot: A) Fe v/s H, B) Ti C) and Mn peak area. Points colored in brown tones were measured near the surface while the black points correspond to the measurements done deeper in the sample. (For interpretation of the references to color in this figure legend, the reader is referred to the Web version of this article.)

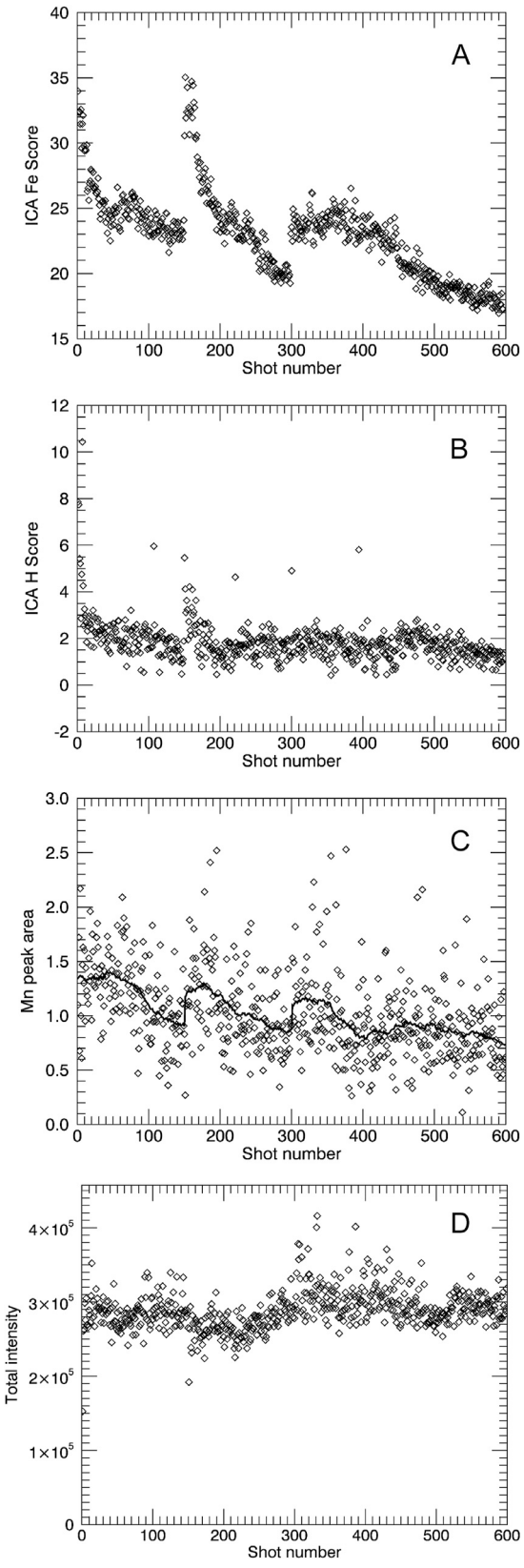

Fig. 8. LIBS measurements of Ferrar dolerite (Depth profile #1). ICA score as a function of shot number for: A) Fe, B) H, C) peak area for Mn (with 50 point running average for Mn) and D) Variation of the total intensity of the signal, after continuum removal. The sudden jumps in signal for Fe, H and Mn at shot number 150 and 300 correspond to a jitter in the laser beam which resampled the fresh surface around the first crater. No such discontinuity is observed at shot #450.

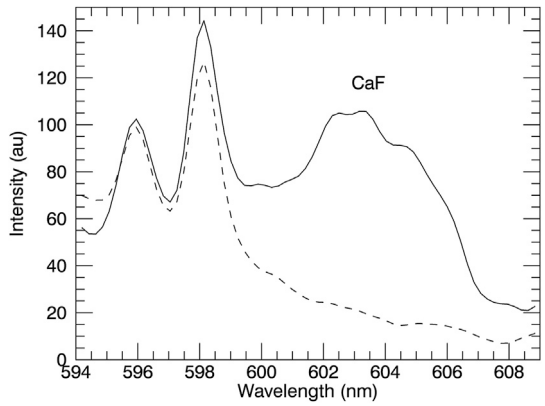

Fig. 9. CaF molecular band observed by LIBS at the surface of the sample: average of the 10 first spectra of the first depth profile (solid line), compared to a spectrum (averaged over 150 shots) acquired in the interior of the sample (dashed line).

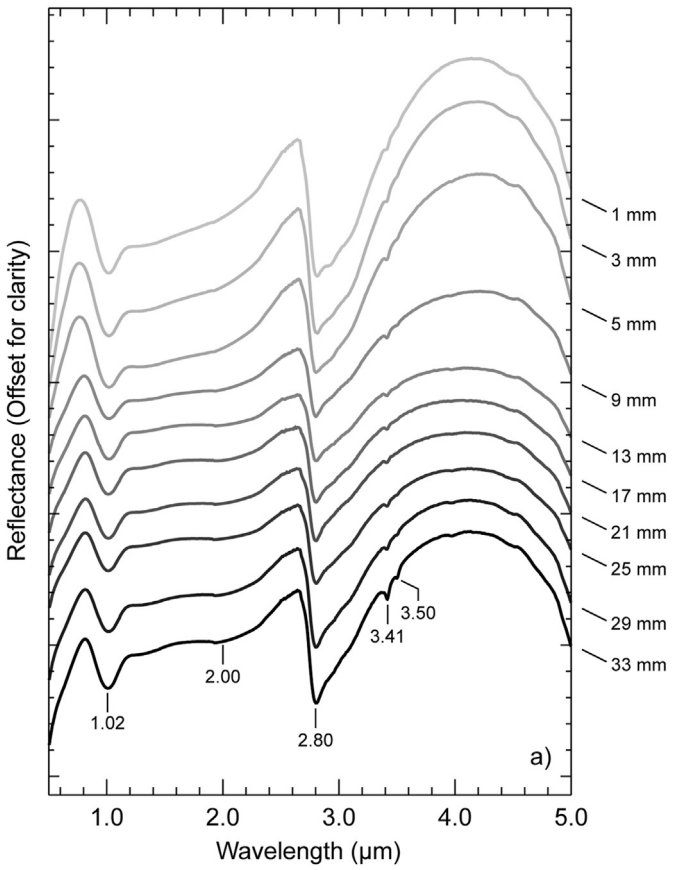

Fig. 10. Reflectance spectra acquired between 0.75 and 5.00 μm of the Ferrar dolerite samples collected at different depths along a weathering profile. Spectra have been offset by 0.5% for clarity. The centre of the main absorption bands is indicated.

4. Discussion on mineralogy and spectral correlations

There is a significant spectral change in the sample between the 3 mm and 9 mm depths which is consistent with the evolution of the main elements that have been analysed. From the sample surface to the core: i) the drop-off of reflectance is less steep in the near infrared and the position of the maximum moves from 0.77 to 0.82 μm, ii) the slope between 1.2 and 2.5 μm decreases and iii) the pyroxene bands are more

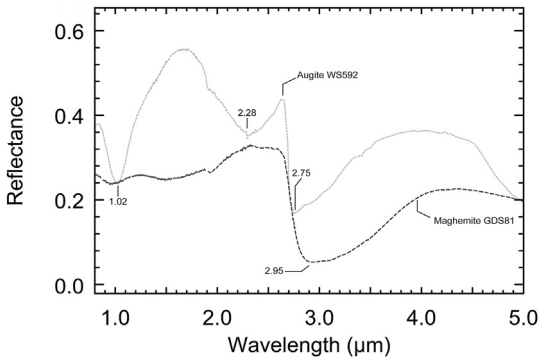

Fig. 11. USGS spectra showing the absorption features of the minerals showing a response in both Vis-NIR and SWIR ranges and that were identified in the Ferrar dolerite: Augite WS592 and Maghemite GDS81(Kokaly et al., 2017)).

pronounced in the discoloration zone (3 and 5 mm deep, Fig. 12C and D and 14C). The spectral measurements done in the discolored zone between 3 and 5 mm (e.g. in the dark zone on Fig. 12C) exhibit an increase of the hydration and pyroxene bands (Figs. 14 and 16), which are probably due to the relative increase of the pyroxene and feldspar content as a result of the dissolution/alteration of the glass matrix, as evidenced by the slight decrease of SiO_2 (Fig. 15B). This confirms the existence of a transition zone between the fresh rock core and the surface rind, where elements are remobilized.

This trend seems to be only inverted in the first millimeter of the sample where the pyroxenes feature area decreases (Fig. 14C) and the water band area does not increase anymore (similarly to the measured H_2O but contrary to the LOI, e.g. Fig. 16B and C). The destabilization of pyroxene is confirmed by the decrease of Ca and Mg (Fig. 15B), which corroborates the migration of divalent cations observed by previous studies (Salvatore et al., 2013). The behaviour of the first sample (i.e. 1 mm deep) is consistent with the presence of an iron and manganese oxide surface rind, which spectrally attenuates the absorption features of clinopyroxene. All these observations are also confirmed by LIBS measurements (Section 2.2), which are sampled at a depth inferior to 1 mm (so only in the surface rind and maybe slightly below), and indicate a decrease of ferro-magnesian component in the first 100–200 μm of the surface LIBS measurements show that plagioclase is fairly resistant to alteration, while pyroxene is progressively replaced by iron (oxy)-hydroxides, thus explaining the loss of Ca and Mg, concomitant to the increase of Fe in the first millimeter. The strong enrichment in hydrogen in the first shots, e.g. close to the surface (Fig. 8B), and the correlation between iron and hydrogen (Fig. 7A), also suggest replacement by iron (oxy)-hydroxides. The first LIBS profile also shows a decrease of Mn with depth (Fig. 7C), but the lack of a clear Fe–Mn correlation (Fig. 7C) suggests that the two elements are not carried by the same phase, and that they have different distribution with depth. The second LIBS depth profile (not shown) also shows a clear Fe-enrichment in the first shots, but no Mn-enrichment, which indicates that the Mn-rich patina is probably patchy at the surface of the sample, unlike the iron (oxy)-hydroxides.

However, these small element fluctuations do not have a significant impact on mineralogical and chemical changes at a larger scale as evidenced by the relatively homogeneous elemental maps (Fig. 3). Although spectroscopically and visually distinct, the surface rind and underlying discolored zone are mineralogically very similar and subtle changes in mineralogical content (e.g. the formation of relatively scarce iron (oxy)-hydroxides) can explain relatively significant changes in spectroscopic properties.

Based on IR spectra alone it is difficult to determine the exact nature of the ferric iron bearing phases occurring in the alteration layer. The alteration products seem to hide the Fe^{3+} absorption band as there is no apparent response near 0.86 μm. Such results are in accordance with the

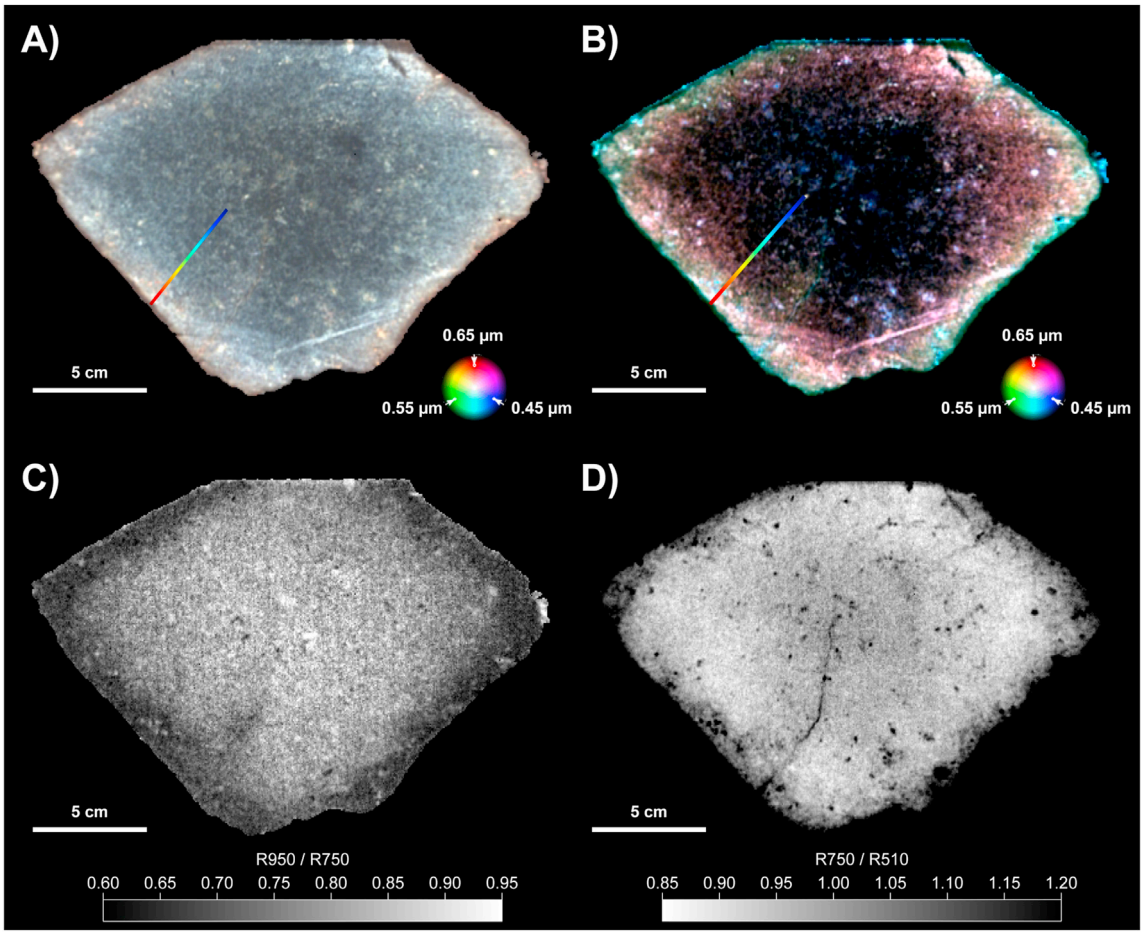

Fig. 12. Ferrar dolerite sample scanned with the HySpex hyperspectral cameras: A) true color composite (red: 0.65 µm, green: 0.55 µm, blue: 0.45 µm), B) false color composite (red: 0.51 µm, green: 0.73 µm, blue: 0.93 µm). Spectra collected along the profile highlighted by a rainbow color bar are presented in Fig. 13 C and D, Band ratios maps calculated to highlight the spectral differences between the surface rind and the fresh zone of the Ferrar dolerite sample: C) R950/R750, D) R750/R510. (For interpretation of the references to color in this figure legend, the reader is referred to the Web version of this article.)

presence of maghemite as identified by XRD, rather than common hematite (Clark et al., 1993). The presence of maghemite in the Ferrar dolerite sample was previously inferred from magnetic measurements (Chevrier et al., 2006a). This "maghemite" may be a specific variety, probably nanocrystalline, as it could not be identified using electron microscopy. But considering that infrared or XRD measurements were done on powders of the bulk rock, this suggests that maghemite concentrates in the rock matrix. The strong correlation between iron and hydrogen in the surface rind suggests the presence of a (oxy)-hydroxide phase, thus different from pure maghemite or hematite which are both devoid of hydroxyl groups. Our results suggest the possibility of hydromaghemite, which has been suggested as an intermediate between ferrihydrite and hematite (Barrón et al., 2003; Liu et al., 2008). This phase destabilizes fairly quickly into hematite in the previously studied hydrothermal environments, but could be metastable at much longer timescales due to the much colder and arid environment prevailing in Antarctica. This phase would also be different from the titanomaghemite previously observed (Chevrier et al., 2006a), which is essentially oxidized titanomagnetite inherited from the primary basaltic rock, and is probably responsible for the correlation between iron and titanium observed by LIBS (Fig. 7B). The increase of such correlation close to the surface is probably due to the preferential dissolution of the glass matrix and the pyroxenes in the first few hundred microns. ESEM observations suggest that the same iron (oxy)-hydroxides also concentrate in discrete veins open to the atmosphere (Figs. 3 and 4). Even with a 1 mm-thick sample, and considering that the rind is probably extremely thin as a result of slow alteration and aeolian erosion, the bands of pyroxene are significantly attenuated.

Previous studies showed that phyllosilicates are often present in desert coatings and varnishes (Potter and Rossman, 1977). Despite their presence in the surface rind XRD analyses (peak at $2\theta = 12°$, Fig. 2), no well-developed phyllosilicate absorption band such as 1.40, 1.90 and 2.20–2.30 µm features could be observed on the Ferrar dolerite infrared reflectance spectra. This could be due to a cryptocrystalline nature of these weathering products (i.e. grain size lower than the analytical wavelength). Another explanation would be that due to the slow weathering kinetics, aeolian activity can effectively remove the phyllosilicates from the surface which would explain the presence of an extremely thin varnish on top of the weathered rind and the presence of clay minerals in soils derived from the Ferrar dolerite alteration (McAdam et al., 2004; Salvatore et al., 2013). However, we did not observe any phyllosilicate in the alteration veins, yet they are filled with iron (oxy)-hydroxides. Therefore, an important characteristic of recent cold weathering is that it does not produce substantial phyllosilicates coatings or varnishes, at least in the alteration profile we have characterized.

Together with the detection of chlorine by EDAX and the presence of sodium chloride on the surface and in the connected veins of the sample (see Fig. 3 and also Fig. 3H in Chevrier et al., 2006a), the detection of fluorine by LIBS measurements (Fig. 9) indicates a chemical overprint originating from the oceanic environment (Bao et al., 2008). This surface enrichment, only seen in the first depth profile, probably results from the (non-uniform) deposition of marine aerosols, which constitute one of the major natural sources of airborne fluoride, after volcanic eruptions and geysers (Lewandowska et al., 2013; Mahadevan et al., 1986). The

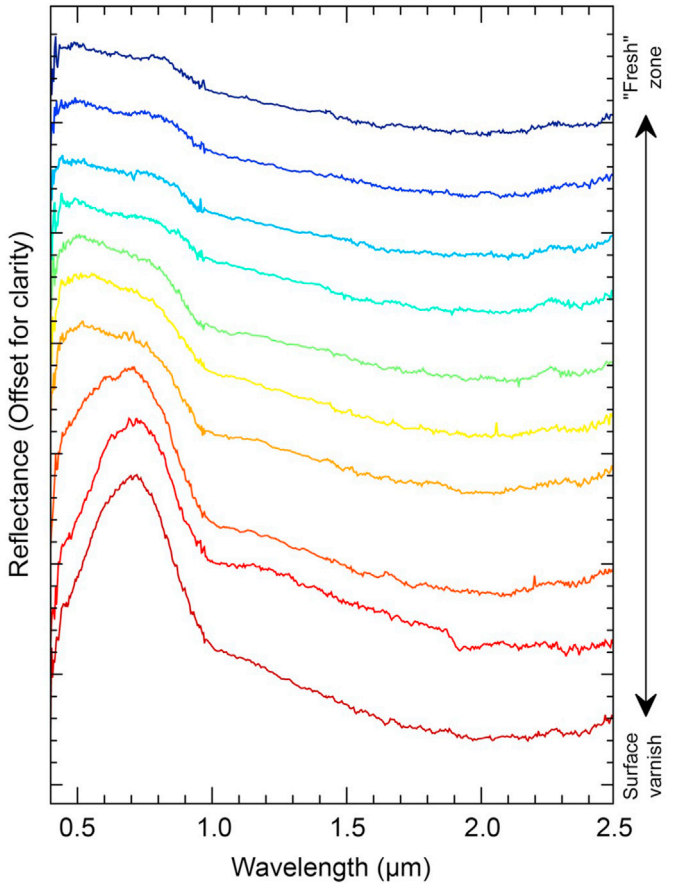

Fig. 13. Spectra collected on the hyperspectral data cube along a profile from the surface rind (red) to the fresh rock zone (blue). Spectra have been offset by 0.5% for clarity. The location of the spectra on the hyperspectral image is indicated by the rainbow color bar presented in Fig. 12A and B. (For interpretation of the references to color in this figure legend, the reader is referred to the Web version of this article.)

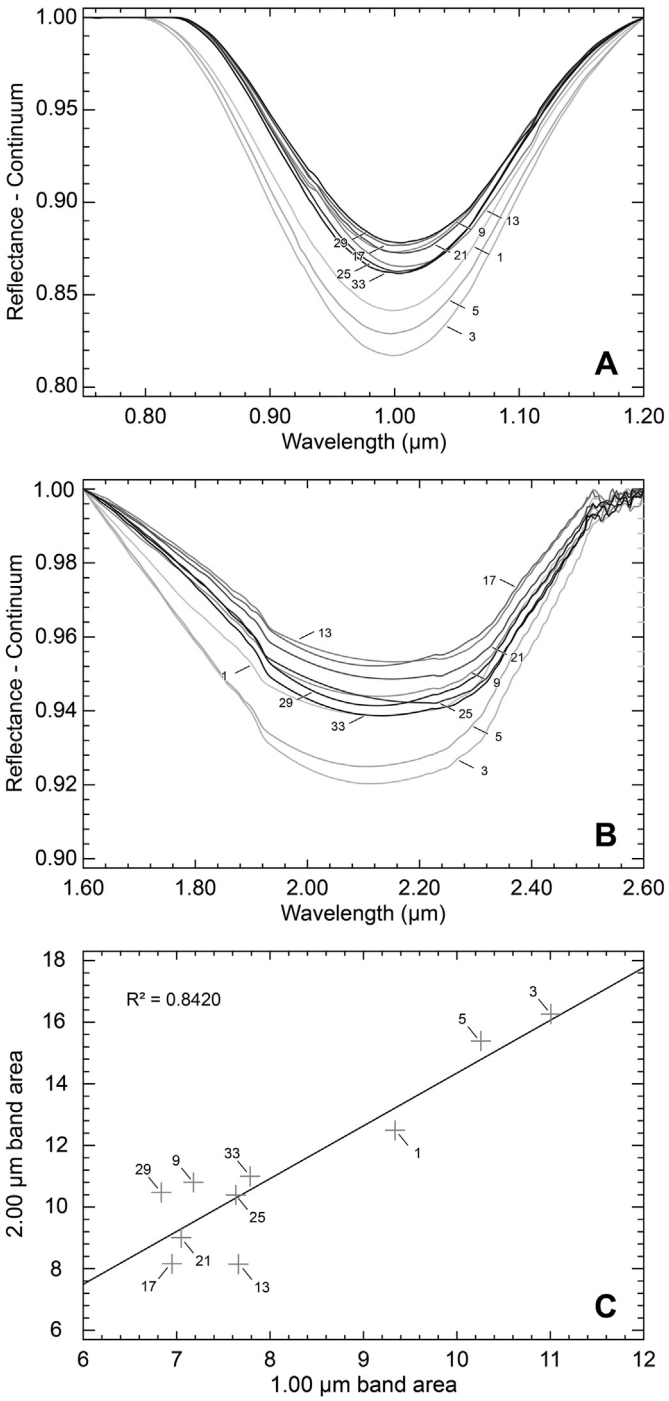

Fig. 14. Continuum removed spectra between 0.75 and 1.20 μm (A) and 1.60–2.60 μm (B) showing the evolution of the 1.00 and 2.00 μm bands respectively. Scatterplots showing the band depth v/s band area (C) and the 1.00 μm v/s 2.00 μm band area (D). The numbered labels indicate the sample depth (in mm) for each powder spectra.

presence of fluorine may indicate a quite recent deposition or a very dry environment, as degasification of hydrofluoric acid (HF) from marine aerosols occurs readily when they react with acids, and F is expected to be depleted in aged marine aerosols at high relative humidities (Brimblecombe and Clegg, 1988). Altogether, these results indicates a chemical overprint probably originating from the oceanic environment (Bao et al., 2008) and partially responsible for the alteration at the surface of the sample or in the interior veins connected to the surface (e.g. presence of chlorine and fluorine). However, the general mineralogical trends observed along the weathering profiles are largely explained by oxidative "dry" weathering, as indicated by the presence of metastable maghemite in the interior of the rock.

5. Conclusions and implications for Mars exploration

The present study shows that alteration/weathering, in cold and dry climate relatively similar to what is expected on Mars, produces only subtle changes in chemistry and mineralogy, essentially characterized by the formation of iron (oxy)-hydroxides at the expense of ferromagnesian minerals (e.g. pyroxene). A strong spectral correlation was observed between the spectral properties and the mineralogy/chemistry. The 1.00 and 2.00 μm bands are good indicators of FeO contents. The anti-correlation observed in the first millimeter (i.e. where the band areas are slightly lower while the iron content increases) could be related to a change in oxidation from FeO to Fe_2O_3 resulting from the accumulation of ferric (oxy)-hydroxides. The strong correlation with the LOI (hydration) suggests that the 2.80 μm band could be used as an alteration index of the rock surface. Nevertheless, this study demonstrates that the very thin rind covering the rock in such environments can alter the spectral signature of the primary rock, while the overall mineralogical and chemical composition remains relatively unaltered. Considering the small variation of concentration of different elements between the core and the surface (less than 4%), the spectral results presented by this study show that the spectroscopic properties are sensitive to slight but significant composition variations, and therefore to the degree of alteration of

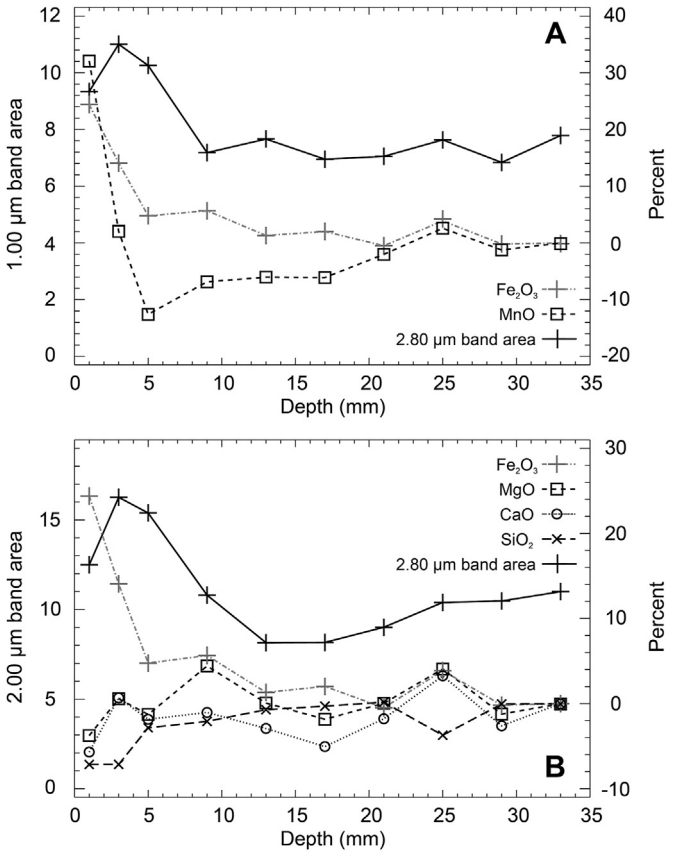

Fig. 15. Evolution of both the 1.00 µm (A) and the 2.00 µm (B) band area (the black cross profile refers to the left Y axis) and the relative concentrations of various major elements (right Y axis) as a function of depth along the drill core (from Chevrier et al., 2006a). Element percentages are normalized to the value of the core as $(X_{core}-X_{depth})/X_{core}$. The reference values are provided in Chevrier et al. (2006a) (Table 1). But as an example, iron values vary from 10.51 wt% Fe_2O_3 at 33 mm to 13.08 wt% Fe_2O_3 in the first mm.

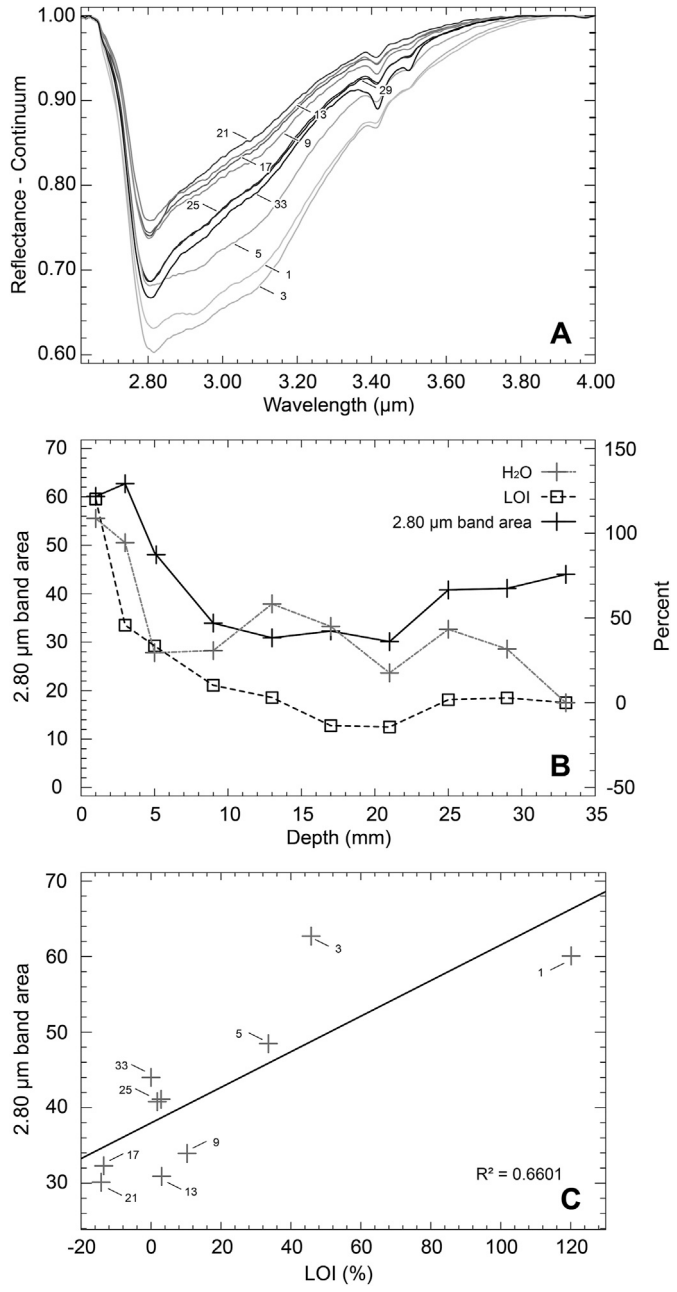

Fig. 16. Continuum removed spectra between 2.60 and 4.00 µm (A). Evolution of the 2.80 µm band area (the black cross profile refers to the left Y axis) and both the H_2O and the LOI relative concentrations normalized to the core values (right Y axis) as a function of the sample depth (B) (from Chevrier et al., 2006a). Scatterplots showing the LOI (%) v/s the 2.80 µm band area (C).

rocks. That said, this study confirms the results of previous studies conducted in Antarctica (Salvatore et al., 2013, 2014) and on Mars (Hurowitz and McLennan, 2007; Salvatore et al., 2019). They show that weathering in cold and dry environments proceeds at almost constant mineralogical and geochemical composition. One of the most significant mineralogical by-product of such alteration pathway is the formation of red and magnetic nanophase iron (oxy)-hydroxides, most probably (hydro)maghemite, accompanied by titanomagnetite/titanomaghemite inherited from the parent rock, very similar to what has been previously observed on Mars (Goetz et al., 2005). Further aeolian erosion of the even micrometer-sized alteration varnishes would probably be enough to produce the red dust covering the entire planet and exhibiting these unusual magnetic properties. The scarcity of igneous rocks found in Gale crater, where rocks are predominantly sedimentary rocks (mudstones, fine-grained sandstones) altered by diagenetic fluids, and conglomerates eroded by fluvial transport, does not make it the most ideal place on Mars to identify the signature of such an alteration pathway. However, in other locations with greater access to igneous lithologies, it would be interesting to compare the infrared spectral signature of altered rocks with the spectral response acquired in recent impact craters where alteration and dust have not affected the signature of the basaltic rocks which remain unaltered. The payload of the forthcoming Mars 2020 "Perseverance" rover will include the use of DRX, LIBS, infrared and Raman spectroscopy. In particular, the SuperCam instrument might prove very diagnostic to go one step further compared to previous analyses. It will provide the possibility to acquire collocated measurements of LIBS (typically performing rasters of 1 × 5 or 1 × 10 points containing 30 laser shots each, or depth profiles with up to 600 collocated shots), Raman, and passive infrared spectroscopy covering for the first time in situ on Mars the very diagnostic 1.30–2.60 µm wavelength range, in areas where the dust will be removed by the LIBS laser shots. It has also the capability to analyse the inner walls of drill holes and the interior of rocks broken by the wheels of the rover. Looking for chemical gradients between the surface of rocks and their interior, or within depth profiles as done in the current study, could reveal how cold and dry weathering modified the chemical and mineralogical composition of Martian igneous rocks.

CRediT authorship contribution statement

V.F. Chevrier: Conceptualization, Investigation, Formal analysis, Writing - original draft. **R. Roy:** Formal analysis, Writing - original draft,

Visualization. **P.Y. Meslin:** Formal analysis, Writing - review & editing, Visualization. **S. Le Mouélic:** Writing - review & editing. **P.E. Mathé:** Supervision. **P. Rochette:** Supervision. **G. Bonello:** Methodology.

Declaration of competing interest

The authors declare that they have no known competing financial interests or personal relationships that could have appeared to influence the work reported in this paper.

Acknowledgements

The authors would like to thank the PNRA (Programmo Nazionale di Ricerca in Antartide,Italian Antarctic program) and A. Meloni from INGV Roma for providing the studied sample. P.-Y. Meslin acknowledges support from the Agence Nationale de la Recherche (ANR) under the program ANR-16-CE31-0012 entitled "MarsPRIME" for the LIBS analyses. Funding for the Engineering Model of ChemCam used for the LIBS experiment was provided by the Centre National d'Etudes Spatiales (CNES) and by Los Alamos National Laboratory (LANL). We thank two anonymous reviewers who helped improve this manuscript.

Appendix A. Supplementary data

Supplementary data to this article can be found online at https://doi.org/10.1016/j.pss.2020.105106.

References

Adams, J.B., McCord, T.B., 1972. Electronic spectra of pyroxenes and interpretation of telescopic spectral reflectivity curves of the Moon. In: Third Lunar and Planetary Science Conference, vol. 3. Geochimica et Cosmochimica Acta, Houston, Texas, pp. 3021–3034.

Allen, C.C., Conga, J.L., 1991. Weathering of basaltic rocks under cold, arid conditions : Antarctica and Mars (abstract). Proceedings of Lunar and Planetary Science 21, 711–717.

Bandfield, J.L., Hamitlon, V.E., Christensen, P.R., 2000. A global view of Martian surface compositions from MGS-TES. Science 287, 1626–1630.

Banin, A., Ben-Schlomo, T., Margulies, L., Blake, D.F., Mancinelli, L., Gehring, E.U., 1993. The nanophase iron mineral(s) in Mars soil. J. Geophys. Res. 98 (E11), 20831–20853.

Bao, H., Barnes, J.D., Sharp, Z.D., Marchant, D.R., 2008. Two chloride sources in soils of the McMurdo Dry Valleys, Antarctica. J. Geophys. Res.: Atmosphere 113 (D3).

Barrón, V., Torrent, J., De Grave, E., 2003. Hydromaghemite, an intermediate in the hydrothermal transformation of 2-line ferrihydrite into hematite. Am. Mineral. 88 (11–12), 1679–1688.

Bell III, J.F., McSween Jr., H.Y., Crisp, J.A., Morris, R.V., Murchie, S.L., Bridges, N.T., Johnson, J.R., Britt, D.T., Golombek, M.P., Moore, H.J., Ghosh, A., Bishop, J.L., Anderson, R.C., Brückner, J., Economou, T., Greenwood, J.P., Gunnlaugsson, H.P., Hargraves, R.M., Hviid, S., Knudsen, J.M., Madsen, M.B., Reid, R., Rieder, R., Soderblom, L., 2000. Mineralogic and compositional properties of Martian soil and dust : results from Mars Pathfinder. J. Geophys. Res. 105 (E1), 1721–1755.

Bender Koch, C., Morup, S., Madsen, M.B., Vistisen, L., 1995. Iron-containing products of basalt in a cold-dry climate. Chem. Geol. 122, 109–119.

Bibring, J.P., Langevin, Y., Mustard, J.F., Poulet, F., Arvidson, R., Gendrin, A., Gondet, B., Mangold, N., Pinet, P., Forget, F., team, t.O., 2006. Global mineralogical and aqueous Mars history derived from OMEGA/Mars express data. Science 312, 400–404.

Bish, D.L., Blake, D.F., Vaniman, D.T., Chipera, S.J., Morris, R.V., Ming, D.W., Treiman, A.H., Sarrazin, P., Morrison, S.M., Downs, R.T., Achilles, C.N., Yen, A.S., Bristow, T.F., Crisp, J.A., Morookian, J.M., Farmer, J.D., Rampe, E.B., Stolper, E.M., Spanovich, N., Team, M.S.L.S., 2013. X-ray diffraction results from Mars science laboratory: mineralogy of rocknest at Gale crater. Science 341 (6153). https://doi.org/10.1126/science.1238932.

Bishop, J.L., Fröschl, H., Mancinelli, R.L., 1998. Alteration processes in volcanic soils and identification of exobiologically important weathering products on Mars using remote sensing. J. Geophys. Res. 103 (E13), 31457–31476.

Bishop, J.L., Pieters, C.M., Burns, R.G., Edwards, J.O., Mancinelli, R.L., Fröschl, H., 1995. Reflectance spectroscopy of ferric sulfate-bearing montmorillonites as Mars soil analog materials. Icarus 117, 101–119.

Blake, D.F., Morris, R.V., Kocurek, G., Morrison, S.M., Downs, R.T., Bish, D., Ming, D.W., Edgett, K.S., Rubin, D., Goetz, W., Madsen, M.B., Sullivan, R., Gellert, R., Campbell, I., Treiman, A.H., McLennan, S.M., Yen, A.S., Grotzinger, J., Vaniman, D.T., Chipera, S.J., Achilles, C.N., Rampe, E.B., Sumner, D., Meslin, P.Y., Maurice, S., Forni, O., Gasnault, O., Fisk, M., Schmidt, M., Mahaffy, P., Leshin, L.A., Glavin, D., Steele, A., Freissinet, C., Navarro-GonzÃ¡lez, R., Yingst, R.A., Kah, L.C., Bridges, N., Lewis, K.W., Bristow, T.F., Farmer, J.D., Crisp, J.A., Stolper, E.M., Des Marais, D.J., Sarrazin, P., Team, M.S.L.S., 2013. Curiosity at Gale crater, Mars: characterization and analysis of the rocknest sand shadow. Science 341 (6153). https://doi.org/10.1126/science.1239505.

Brimblecombe, P., Clegg, S., 1988. The solubility and behaviour of acid gases in the marine aerosol. J. Atmos. Chem. 7 (1), 1–18.

Campbell, I.B., Claridge, G., 1987. Antarctica: Soils, Weathering Processes and Environment. Elsevier.

Cannon, K.M., Mustard, J.F., Salvatore, M.R., 2015. Alteration of immature sedimentary rocks on Earth and Mars: recording aqueous and surface–atmosphere processes. Earth Planet Sci. Lett. 417, 78–86.

Chevrier, V., Mathé, P.E., Rochette, P., Gunnlaugsson, H.P., 2006a. Magnetic study of an antarctic weathering profile on basalt: implications for recent weathering on Mars. Earth Planet Sci. Lett. 244, 501–514.

Chevrier, V., Rochette, P., Mathé, P.-E., Grauby, O., 2004. Weathering of iron rich phases in simulated Martian atmospheres. Geology 32 (12), 1033–1036.

Chevrier, V., Roy, R., Le Mouélic, S., Borschneck, D., Mathé, P.E., Rochette, P., 2006b. Spectral characterization of weathering products of elemental iron in a Martian atmosphere: implications for Mars hyperspectral studies. Planet. Space Sci. 54 (11), 1034–1045.

Chide, B., Maurice, S., Murdoch, N., Lasue, J., Bousquet, B., Jacob, X., Cousin, A., Forni, O., Gasnault, O., Meslin, P.-Y., 2019. Listening to laser sparks: a link between Laser-Induced Breakdown Spectroscopy, acoustic measurements and crater morphology. Spectrochim. Acta B Atom Spectrosc. 153, 50–60.

Clark, R.N., Roush, T.L., 1984. Reflectance spectroscopy: quantitative analysis techniques for remote sensing applications. J. Geophys. Res. 89, 6329–6340.

Clark, R.N., Swayze, G.A., Gallagher, A.J., King, T.V.V., Calvin, W.M., 1993. The U.S. Geological Survey, Digital Spectral Library: Version 1: 0.2 to 3.0 Microns. U.S. Geological Survey Open File Report, pp. 93–592.

Clegg, S.M., Wiens, R.C., Anderson, R., Forni, O., Frydenvang, J., Lasue, J., Cousin, A., Payre, V., Boucher, T., Dyar, M.D., 2017. Recalibration of the Mars science laboratory ChemCam instrument with an expanded geochemical database. Spectrochim. Acta B Atom Spectrosc. 129, 64–85.

Comon, P., 1994. Independent component analysis, a new concept? Signal Process. 36 (3), 287–314.

Cousin, A., 2012. LIBS (Laser-Induced Breakdown Spectroscopy) Pour L'observation Martienne. Université Paul Sabatier-Toulouse III.

Cousin, A., Forni, O., Maurice, S., Gasnault, O., Fabre, C., Sautter, V., Wiens, R.C., Mazoyer, J., 2011. Laser induced breakdown spectroscopy library for the Martian environment. Spectrochim. Acta B Atom Spectrosc. 66 (11–12), 805–814. https://doi.org/10.1016/j.sab.2011.10.004.

Dehouck, E., Chevrier, V., Gaudin, A., Mangold, N., Mathé, P.E., Rochette, P., 2012. Evaluating the role of sulfide-weathering in the formation of sulfates or carbonates on Mars. Geochem. Cosmochim. Acta 90, 47–63.

Dehouck, E., McLennan, S.M., Meslin, P.Y., Cousin, A., 2014. Constraints on abundance, composition, and nature of X-ray amorphous components of soils and rocks at Gale crater, Mars. J. Geophys. Res.: Plan 119 (12), 2640–2657.

Dequaire, T., Meslin, P.-Y., Beck, P., Jaber, M., Cousin, A., Rapin, W., Lasne, J., Gasnault, O., Maurice, S., Buch, A., 2017. Analysis of carbon and nitrogen signatures with laser-induced breakdown spectroscopy; the quest for organics under Mars-like conditions. Spectrochim. Acta B Atom Spectrosc. 131, 8–17.

Dickinson, W.W., Rosen, M.R., 2003. Antarctic permafrost: an analogue for water and diagenetic minerals on Mars. Geology 31 (3), 199–202.

Effenberger, A.J., Scott, J.R., 2010. Effect of atmospheric conditions on LIBS spectra. Sensors 10 (5), 4907–4925.

Elliot, D., Fleming, T., Haban, M., Siders, M., 1995. Petrology and mineralogy of the kirkpatrick basalt and ferrar dolerite, mesa range region, north victoria land, Antarctica. Contributions to Antarctic Research IV 67, 103–141.

Folco, L., d'Orazio, M., Gemelli, M., Rochette, P., 2016. Stretching out the australasian microtektite strewn field in victoria land transantarctic mountains. Polar Science 10 (2), 147–159.

Folco, L., Rochette, P., Perchiazzi, N., D'Orazio, M., Laurenzi, M., Tiepolo, M., 2008. Microtektites from Victoria land transantarctic mountains. Geology 36 (4), 291–294.

Forni, O., Maurice, S., Gasnault, O., Wiens, R.C., Cousin, A., Clegg, S.M., Sirven, J.-B., Lasue, J., 2013. Independent component analysis classification of laser induced breakdown spectroscopy spectra. Spectrochim. Acta B Atom Spectrosc. 86, 31–41.

Gavin, P., Chevrier, V., 2010. Thermal alteration of nontronite and montmorillonite: implications for the martian surface. Icarus 208 (2), 721–734.

Goetz, W., Bertelsen, P., Binau, C.S., Gunnlaugsson, H.P., Hviid, S.F., Kinch, K.M., Madsen, D.E., Madsen, M.B., Olsen, M., Gellert, R., Klingelhöfer, G., Ming, D.W., Morris, R.V., Rieder, R., Rodionov, D.S., de Souza Jr., P.A., Schröder, C., Squyres, S.W., Wdowiak, T., Yen, A., 2005. Indication of drier periods on Mars from the chemistry and mineralogy of atmospheric dust. Nature 436, 62–65.

Goetz, W., Pike, W.T., Hviid, S.F., Madsen, M.B., Morris, R.V., Hecht, M.H., Staufer, U., Leer, K., Sykulska, H., Hemmig, E., Marshall, J., Morookian, J.M., Parrat, D., Vijendran, S., Bos, B.J., El Maarry, M.R., Keller, H.U., Kramm, R., Markiewicz, W.J., Drube, L., Blaney, D., Arvidson, R.E., Bell III, J.F., Reynolds, R., Smith, P.H., Woida, P., Woida, R., Tanner, R., 2010. Microscopy analysis of soils at the Phoenix landing site, Mars: classification of soil particles and description of their optical and magnetic properties. J. Geophys. Res. 115 (E00E22) https://doi.org/10.1029/2009JE003437.

Gunn, B.M., 1962. Differenciation in ferrar dolerites, antartica. N. Z. J. Geol. Geophys. 5, 820–863.

Hunt, G.R., Salisbury, J.W., 1970. Visible and near-infrared spectra of minerals and rocks : I. Silicate minerals. Mod. Geol. 1, 283–300.

Hurowitz, J.A., McLennan, S.M., 2007. Â 3.5 Ga record of water-limited, acidic weathering conditions on Mars. Earth Planet Sci. Lett. 260 (3–4), 432–443.

Hyvärinen, A., Hoyer, P.O., Inki, M., 2001. Topographic independent component analysis. Neural Comput. 13 (7), 1527–1558.
Kokaly, R., Clark, R., Swayze, G., Livo, K., Hoefen, T., Pearson, N., Wise, R., Benzel, W., Lowers, H., Driscoll, R., 2017. USGS Spectral Library Version 7 Data. US Geological Survey data release.
Leshin, L., Mahaffy, P., Webster, C., Cabane, M., Coll, P., Conrad, P., Archer, P., Atreya, S., Brunner, A., Buch, A., 2013. Volatile, isotope, and organic analysis of martian fines with the Mars Curiosity rover. Science 341 (6153), 1238937.
Lewandowska, A., Falkowska, L., Jóźwik, J., 2013. Factors determining the fluctuation of fluoride concentrations in PM10 aerosols in the urbanized coastal area of the Baltic Sea (Gdynia, Poland). Environ. Sci. Pollut. Control Ser. 20 (9), 6109–6118.
Liu, Q., Barron, V., Torrent, J., Eeckhout, S.G., Deng, C., 2008. Magnetism of intermediate hydromaghemite in the transformation of 2-line ferrihydrite into hematite and its paleoenvironmental implications. J. Geophys. Res.: Solid Earth 113 (B1).
Mahadevan, T.N., Meenakshy, V., Mishra, U.C., 1986. Fluoride cycling in nature through precipitation. Atmos. Environ. 20 (9), 1745–1749, 1967.
Maurice, S., Wiens, R., Saccoccio, M., Barraclough, B., Gasnault, O., Forni, O., Mangold, N., Baratoux, D., Bender, S., Berger, G., 2012. The ChemCam instrument suite on the Mars Science Laboratory (MSL) rover: science objectives and mast unit description. Space Sci. Rev. 170 (1–4), 95–166.
McAdam, A.C., Leshin, L.A., Harvey, R.P., Hoffman, E.J., 2004. Antarctic soil derived from the Ferrar dolerite and implications for the formation of martian surface materials. In: Second Conference on Early Mars: Geologic, Hydrologic, and Climatic Evolution and the Implications for Life abstract #8050, Jackson Hole, Wyoming.
Merchel, S., Benedetti, L., Bourlès, D., Braucher, R., Dewald, A., Faestermann, T., Finkel, R., Korschinek, G., Masarik, J., Poutivtsev, M., 2010. A multi-radionuclide approach for in situ produced terrestrial cosmogenic nuclides: 10Be, 26Al, 36Cl and 41Ca from carbonate rocks. Nucl. Instrum. Methods Phys. Res. Sect. B Beam Interact. Mater. Atoms 268 (7–8), 1179–1184.
Meslin, P.Y., Gasnault, O., Forni, O., Schroder, S., Cousin, A., Berger, G., Clegg, S.M., Lasue, J., Maurice, S., Sautter, V., Le MouÃ©lic, S., Wiens, R.C., Fabre, C., Goetz, W., Bish, D., Mangold, N., Ehlmann, B., Lanza, N., Harri, A.M., Anderson, R., Rampe, E., McConnochie, T.H., Pinet, P., Blaney, D., Leveille, R., Archer, D., Barraclough, B., Bender, S., Blake, D., Blank, J.G., Bridges, N., Clark, B.C., DeFlores, L., Delapp, D., Dromart, G., Dyar, M.D., Fisk, M., Gondet, B., Grotzinger, J., Herkenhoff, K., Johnson, J., Lacour, J.L., Langevin, Y., Leshin, L., Lewin, E., Madsen, M.B., Melikechi, N., Mezzacappa, A., Mischna, M.A., Moores, J.E., Newsom, H., Ollila, A., Perez, R., Renno, N., Sirven, J.B., Tokar, R., de la Torre, M., d'Uston, L., Vaniman, D., Yingst, A., Team, M.S.L.S., 2013. Soil diversity and hydration as observed by ChemCam at Gale crater, Mars. Science 341 (6153). https://doi.org/10.1126/science.1238670.
Milliken, R.E., Mustard, J.F., 2007a. Estimating the water content of hydrated minerals using reflectance spectroscopy. I. Effects of darkening agents and low-albedo materials. Icarus 189 (2), 550–573.
Milliken, R.E., Mustard, J.F., 2007b. Estimating the water content of hydrated minerals using reflectance spectroscopy. II. Effects of particle size. Icarus 189 (2), 574–588.
H. V. L Morris, R.V., Agresti Jr., D.G., Newcomb, J.A., Shelfer, T.D., Murali, A.V., 1989. Evidence for pigmentary hematite on Mars based on optical, magnetic, and Mössbauer studies of superparamagnetic (nanocrystalline) hematite. J. Geophys. Res. 94 (B3), 2760–2778.
Morris, R.V., Golden, D.C., 1998. Goldenrod pigments and the occurrence of hematite and possibly goethite in the Olympus-Amazonis Region of Mars. Icarus 134 (1), 1–10.
Morris, R.V., Klingelhöfer, G., Bernhardt, B., Schröder, C., Rodionov, D.S., de Souza Jr., P.A., Yen, A., Gellert, R., Evlanov, E.N., Foh, J., Kankeleit, E., Gütlich, P., Ming, D.W., Renz, F., Wdowiak, T., Squyres, S.W., Arvidson, R.E., 2004. Mineralogy at gusev crater from the mössbauer spectrometer on the spirit rover. Science 305 (5685), 833–836.
Newsom, H.E., Hagerty, J.J., Goff, F., 1999. Mixed hydrothermal fluids and the origin of the Martian soil. J. Geophys. Res. 104 (E4), 8717–8728.
Nolin, A.W., Dozier, J., 2000. A hyperspectral method for remotely sensing the grain size of snow. Remote Sens. Environ. 74, 207–216.
Pommerol, A., Schmitt, B., 2008. Strength of the H2O near-infrared absorption bands in hydrated minerals: effects of particle size and correlation with albedo. J. Geophys. Res. 113 (E10009).
Potter, R.M., Rossman, G.R., 1977. Desert varnish: the importance of clay minerals. Science 196, 1446–1448.
Poulet, F., Gomez, C., Bibring, J.-P., Langevin, Y., Gondet, B., Pinet, P., Belluci, G., Mustard, J., 2007. Martian surface mineralogy from Observatoire pour la Mineralogie, l'Eau, les Glaces et l'Activite on board the Mars Express spacecraft (OMEGA/MEx): global mineral maps. J. Geophys. Res. 112 (E08S02).
Sallé, B., Lacour, J.-L., Mauchien, P., Fichet, P., Maurice, S., Manhes, G., 2006. Comparative study of different methodologies for quantitative rock analysis by laser-induced breakdown spectroscopy in a simulated Martian atmosphere. Spectrochim. Acta B Atom Spectrosc. 61 (3), 301–313.
Salvatore, M., Mustard, J., Head, J., Cooper, R., Marchant, D., Wyatt, M., 2013. Development of alteration rinds by oxidative weathering processes in Beacon Valley, Antarctica, and implications for Mars. Geochem. Cosmochim. Acta 115, 137–161.
Salvatore, M., Mustard, J., Head, J., Rogers, A., Cooper, R., 2014. The dominance of cold and dry alteration processes on recent Mars, as revealed through pan-spectral orbital analyses. Earth Planet Sci. Lett. 404, 261–272.
Salvatore, M., Truitt, K., Roszell, K., Lanza, N., Rampe, E., Mangold, N., Dehouck, E., Wiens, R., Clegg, S., 2019. Investigating the role of anhydrous oxidative weathering on sedimentary rocks in the Transantarctic Mountains and implications for the modern weathering of sedimentary lithologies on Mars. Icarus 319, 669–684. https://doi.org/10.1016/j.icarus.2018.10.007.
Schäfer, J.M., Ivy-Ochs, S., Wieler, R., Leya, I., Baur, H., Denton, G.H., Schlüchter, C., 1999. Cosmogenic noble gas studies in the oldest landscape on earth: surface exposure ages of the Dry Valleys, Antarctica. Earth Planet Sci. Lett. 167 (3–4), 215–226.
Wiens, R.C., Maurice, S., Barraclough, B., Saccoccio, M., Barkley, W.C., Bell, J.F., Bender, S., Bernardin, J., Blaney, D., Blank, J., 2012. The ChemCam instrument suite on the Mars Science Laboratory (MSL) rover: body unit and combined system tests. Space Sci. Rev. 170 (1–4), 167–227.
Zavala, K., Leitch, A.M., Fisher, G.W., 2011. Silicic segregations of the ferrar dolerite sills, Antarctica. J. Petrol. 52 (10), 1927–1964.